

Impacts of Atmospheric Dynamics on Drivers of Observed Winter-Spring Sea-Ice and Snow Thickness at a Coastal Site in East Antarctica

Diana Francis^{1*}, Ricardo Fonseca¹, Narendra Nelli¹, Petra Heil^{2,3,4} Jonathan D. Wille⁵, Irina V. Gorodetskaya⁶, Robert A. Massom^{2,3,7}

¹ Environmental and Geophysical Sciences (ENGEOS) Lab, Earth Sciences Department, Khalifa University, Abu Dhabi, 127788, United Arab Emirates

² Australian Antarctic Division, Department of Climate Change, Energy, the Environment and Water, Kingston, Tasmania, Australia

³ Australian Antarctic Program Partnership, Institute for Marine and Antarctic Studies, University of Tasmania, Hobart, Tasmania, Australia

⁴ Institute Snow and Avalanche Research, Swiss Federal Institute for Forest, Snow and Landscape Research, Davos, Switzerland

⁵ Institute for Atmospheric and Climate Science, ETH Zurich, Zurich, Switzerland

⁶ Interdisciplinary Centre of Marine and Environmental Research, University of Porto, Porto, Portugal

⁷ The Australian Centre for Excellence in Antarctic Science, University of Tasmania, Hobart, Tasmania, Australia

*Correspondence to: diana.francis@ku.ac.ae

Abstract:

Antarctic sea ice and its snow cover play a pivotal role in regulating the global climate system through feedback on both the atmospheric and the oceanic circulations. Understanding the intricate interplay between atmospheric dynamics, mixed-layer properties, and sea ice is essential for accurate future climate change estimates. This study investigates the mechanisms behind the relationship between the atmospheric conditions and observed sea-ice and snow characteristics at a coastal site in East Antarcticasite using *in-situ* measurements in winter-spring 2022. The observed sea-ice thickness peaks at 1.16 m in mid-late October and drops to 0.06 m at the end of November, following the seasonal solar cycle. On the other hand, the snow thickness variability is impacted by atmospheric forcing, with significant contributions from precipitation, Foehn effects, blowing snow, and episodic warm and moist air intrusions, which can lead to changes of up to 0.08 m within a day for a field that is in the range 0.02-0.18 m during July-November 2022. A high-resolution simulation with the Polar Weather Research and Forecasting model for the 14 July atmospheric river (AR), the only intense AR that occurred during the study period, reveals the presence of AR rapids and highlights the effects of katabatic winds from the Antarctic Plateau in

35 slowing down the low-latitude air masses as they approach the Antarctica coastline. The resulting
36 convergence of the two air flows, with meridional wind speeds in excess of 45 m s^{-1} , leads to
37 precipitation rates above 3 mm hr^{-1} around coastal Antarctica. The unsteady wind field in response
38 to the passage of a deep low pressure system with a central pressure that dropped to 931 hPa
39 triggers satellite-derived pack ice drift speeds in excess of 60 km day^{-1} , and promotes the opening
40 up of a polynya in the Southern Ocean around $64^\circ\text{S}, 45^\circ\text{E}$ from 14 to 22 July. Our findings
41 contribute to a better understanding of the complex interactions within the Antarctic climate
42 system, providing valuable insights for climate modeling and future projections.

43

44 **Keywords:**

45 Sea Ice, Snow Thickness, PolarWRF, Atmospheric River, [Katabatic winds](#)[Surface Mass](#)
46 [Balance](#), [Föehn Effects](#), Antarctica

47

48 **1. Introduction**

49 Sea ice, which forms from the freezing of seawater and covers 3-6% of the total surface area
50 of the planet, plays multiple crucial roles in the Earth's climate system and high-latitude
51 ecosystems (Thomas, 2017; Eayrs et al., 2019). Changes in the formation and melt rates, extent,
52 seasonality and thickness of Antarctic sea ice - both in the form of drifting pack ice and less
53 extensive stationary near-shore landfast ice (fast ice) attached to coastal margins, sea floor and
54 grounded icebergs (Fraser et al., 2023) - substantially impact the heat and salinity content of the
55 ocean, and hence the oceanic circulation (e.g., Haumann et al., 2016; Li and Fedorov, 2021). At
56 the same time, breaks in the sea ice such as leads and recurrent and persistent polynyas (Barber
57 and Massom, 2007; Francis et al. 2019, 2020; Fonseca et al., 2023) act as a thermal forcing, ~~with
58 the exposure of ice-free ocean water leading to sensible heat fluxes that can exceed 2000 W m^{-2}~~
59 ~~and heat up the atmosphere aloft~~ (Guest, 2021), directly impacting the atmospheric flow (Trusel
60 et al., 2023; Zhang and Screen, 2021). Both oceanic and atmospheric forcing directly affect sea
61 ice and its spatial extent, seasonality and thickness (Wang et al., 2020; Yang et al., 2021), within
62 a finely-coupled interactive ocean-sea ice-atmosphere system. At the same time, decreases in sea-
63 ice thickness (SIT), sea-ice extent (SIE), and its snow cover have strong potential to impact low-
64 latitude weather patterns (England et al., 2020), disrupt the global surface energy balance (Riihelä
65 et al., 2021), and amplify climate warming at high southern latitudes (Williams et al., 2023),
66 leading to increased sea-ice loss that is likely to be further accelerated by poorly-understood ocean-
67 ice-snow-atmosphere feedback mechanisms (Goosse et al., 2023).

68

69 The Antarctic sea ice-snow system is particularly impacted by two atmospheric processes: (1)
70 strong katabatic winds that cascade seawards off the ice sheet and promote sublimation of the sea
71 ice and its snow cover (Elvidge et al., 2020; Francis et al., 2023); and (2) a number of more
72 ephemeral but influential extreme atmospheric events in the form of atmospheric rivers (ARs;

73 Wille et al., 2025). Foehn effects are an important trigger of surface melting around Antarctica, as
74 the adiabatic compression of the downslope flow can lead to a marked increase in surface
75 temperature in excess of 15 K (Bozkurt et al., 2018), while the associated strong winds can promote
76 iceberg calving events (Miles et al., 2017). An AR is a narrow and highly elongated band of
77 moisture-rich air that originates in the tropics and subtropics and propagates polewards into the
78 mid- and high-latitudes (Wille et al., 2019; Gorodetskaya et al., 2020). ARs are associated with
79 increased humidity and cloudiness, leading to an enhancement of the downward longwave
80 radiation flux ~~while still allowing some of the Sun's shortwave radiation to reach the surface~~
81 ~~(Djouma and Holland, 2021), with~~ ~~t~~he resulting increase in the surface net radiation flux ~~gives~~
82 ~~giving~~ a warming tendency and ~~promotes-promoting~~ surface melting (Gorodetskaya et al., 2013;
83 Francis et al., 2020; Ghiz et al., 2021).

84

85 There are several examples of ARs triggering ice and snow melt around Antarctica: e.g. in the
86 Weddell Sea in 1973 and 2017 (Francis et al., 2020); off the Antarctic Peninsula in March 2015
87 (Bozkurt et al., 2018) and February 2022 (Gorodetskaya et al., 2023); around the Amery Ice Shelf
88 in September 2019 (Francis et al., 2021), in West Antarctica (Francis et al., 2023); and in the Ross
89 Sea (Fonseca et al., 2023). The recent study of Liang et al. (2023) highlights that the largest impact
90 of ARs on sea ice is found on the marginal ice zone, where the SIE reduction may exceed 10%
91 day⁻¹. Reduced coastal offshore SIE may also foster a deeper penetration of the low-latitude air
92 onto the inland ice sheet as it enhances moisture availability, as is the case in the March 2022 “heat
93 wave” in East Antarctica (Wille et al., 2024a,b). While ARs themselves are relatively rare and
94 short-lived in coastal Antarctica, with a frequency of ~3 days year⁻¹ at any given location, the warm
95 and moist air masses they transport can make a substantial contribution to the surface mass balance
96 (SMB) and are linked to extreme precipitation events (Massom et al., 2004; Wille et al. 2021,
97 2025). For example, in East Antarctica, a series of ARs delivered an estimated 44% of the total
98 mean-annual snow accumulation to the high interior ice sheet over an 18-day period in the austral
99 summer of 2001/2 (Massom et al., 2004), and AR-associated rainfall has exceeded 30% of the
100 total annual precipitation (McLennan et al. 2022, 2023). These studies highlight the impacts of
101 extreme weather events on the coupled Antarctic ocean-ice-snow-atmosphere system and stress
102 the need to better understand the role of low-latitude air incursions on the SMB and on the state of
103 both the Antarctic Ice Sheet and its surrounding sea-ice cover - and how these may change in a
104 warming climate.

105

106 The effects of the atmospheric forcing, such as that associated with extreme weather episodes,
107 on the sea-ice-snow-air coupling system can be inferred through the analysis of *in-situ*
108 measurements of SIT and snow thickness (ST). This is achieved in this study through the
109 deployment of ~~Here, we investigate the impact of atmospheric dynamics on variability in both SIT~~
110 ~~and snow thickness (ST) state through analysis of high resolution *in-situ* measurements obtained~~
111 ~~by an autonomous Snow Ice Mass Balance Array (SIMBA) buoy (Jackson et al., 2013), combined~~
112 ~~with atmospheric reanalysis and modeling products. The SIMBA buoy was deployed~~ from July to

113 November 2022 at a coastal fast ice site close to Mawson Station in East Antarctica (67.5912°S,
114 62.8563°E), which will be denoted as “Khalifa SIMBA site on fast ice off Mawson Station”
115 throughout the manuscript. This station is selected as it has amongst the highest AR frequency in
116 the continent, also with a statistically significant positive trend in AR frequency and intensity
117 during 1980-2020 (Wille et al., 2025). The overall aim of this study-work is to further our
118 understanding of the temporal evolution of the thickness and vertical structure of coastal sea ice
119 and its snow cover in East Antarctica, and over a six-month period spanning austral winter through
120 late spring, when ARs are more frequent in the region (Wille et al., 2025). The motivation is to
121 provide new observations and process information that will aid numerical modelling efforts to
122 more accurately simulate the annual cycle of the Southern Ocean sea ice, and observed trends and
123 variability in its distribution (and ultimately thickness; c.f. Eayrs et al., 2019). Such an advance is
124 crucial to helping rectify present low confidence in model projections of future climate and
125 Antarctic sea ice conditions that currently diverge for different models and scenarios (Roach et al.,
126 2020). This study is also timely given the precipitous downward trend in Antarctic sea ice extent
127 (SIE) since 2016 (Parkinson, 2019), an extraordinary record-low annual minimum in February
128 2023 and a sudden departure to major sea-ice deficits through the winters of 2023 and 2024 (Reid
129 et al., 2024). This turn of events suggests that Antarctic sea ice has abruptly shifted into a new
130 low-extent regime (Purich and Doddridge, 2023; Hobbs et al., 2024) due to complex changes in
131 the coupled ocean-ice-snow-atmosphere system that are far from well understood. Much less well
132 known - though no less important - are the thicknesses of the ice and its snow thickness (ST) and
133 whether these are changing. Obtaining more accurate and complete information on the Antarctic
134 SIT distribution and its ST and precipitation rates - and the factors and processes controlling them
135 - is a critical high priority in climate science, particularly in light of climate variability and change
136 (Webster et al., 2018; Meredith et al., 2021).

137
138 Accurate knowledge of SIT, SIE and concentration is needed to estimate sea-ice volume, a field
139 that is more sensitive to climate change than SIE and SIT alone (Liu et al., 2020) and is also directly
140 parameterized in numerical models (Massonnet et al., 2013; Zhang, 2014; Schroeter and Sandery,
141 and that exhibits. Current large uncertainties in these quantities prevent proper model
142 evaluation and undermine confidence in model predictions of future Antarctic sea ice conditions
143 and global weather and climate (Maksym et al. 2008, 2012). Satellite radar and laser altimeters
144 hold the key to large-scale estimation and monitoring of both SIT (e.g., Fonseca et al., 2023) and
145 ST (Kacimi and Kwok, 2020). Kurtz and Markus (2012) used the measurements collected by the
146 Ice, Cloud, and land Elevation Satellite (ICESat) to estimate the ice thickness around Antarctica.
147 A comparison with ship-based observations revealed a mean difference of 0.15 m for the period
148 2003-2008, with a typical SIT of 1-1.5 m. Kacimi and Kwok (2020), using both laser (ICESat-2)
149 and radar (CryoSat-2) altimeter estimates for the period 1 April to 16 November 2019, found the
150 thickest sea ice in the western Weddell Sea sector (predominantly multi-year sea ice), with a mean
151 thickness of 2 m, and the thinnest ice around polynyas in the Ross Sea and off the Ronne Ice Shelf.
152 Coincident use of laser and radar altimetry also enables basin-scale estimates of ST. The thickest

153 snow was again observed in the western Weddell Sea (0.228 ± 12.4 m in May) and the coastal
154 region of the Amundsen-Bellingshausen seas sector (0.314 ± 23.1 m in September), while the
155 thinnest was in the Ross Sea (0.0735 ± 4.30 m in April) and the eastern Weddell Sea
156 (0.0821 ± 5.81 m in June) (Kacimi and Kwok, 2020). These studies focussed on pack ice, but a
157 similar range of values has been estimated for the thickness of fast ice, such as off Mawson (Li et
158 al., 2022) and Davis (Heil, 2006) stations in East Antarctica. The SIMBA buoy ~~provides high-resolution measurements at a given location of the vertical temperature profile through the air-snow ice upper ocean column, from which ST and SIT can be derived and monitored (Jackson et al., 2013)~~. Time series of such point observations provide invaluable gap-filling information on
162 the temporal evolution and state of the snow-sea ice system and its response to atmospheric and
163 oceanic variability. They ~~are also provide crucial information with which~~ to both (1) calibrate the
164 key satellite SIT and ST data products, and (2) evaluate and improve numerical idealized column
165 and weather forecasting models (Hu et al., 2023; Plante et al., 2024; Sledd et al., 2024; Wang et
166 al., 2024a). ~~Such steps are needed to rectify present low confidence in model projections of future~~
167 ~~climate and Antarctic sea-ice conditions that currently diverge for different models and scenarios~~
168 ~~(Roach et al., 2020)~~.
169

170 While there are a number of studies on *in-situ* SIT and ST measurements around Antarctica
171 (e.g., Worby et al., 2011; Xie et al., 2011; Liao et al., 2022), the area of East Antarctica around
172 Mawson Station, where extreme precipitation events in the form of ARs have become more
173 frequent and intense in the recent decades (Wille et al., 2025), has not been sampled. In addition,
174 these works do not delve deep into the processes responsible for the observed changes in SIT and
175 ST, which is a necessary step for refining Antarctic climate projections. The objectives of this
176 study are twofold: (1) to identify the mechanisms behind the variability of the *in-situ* measured
177 SIT and ST at Mawson Station during July-November 2022, and compare the measured values
178 with those estimated from remote sensing assets; and (ii) to perform high-resolution numerical
179 simulations for selected periods during the measurement campaign, in particular during extreme
180 weather events, to gain further insight into the role of atmospheric forcing on the SIT and ST. This
181 study will therefore contribute to further our understanding on the variability of the SIT and ST in
182 coastal Antarctica and the respective driver processes.
183

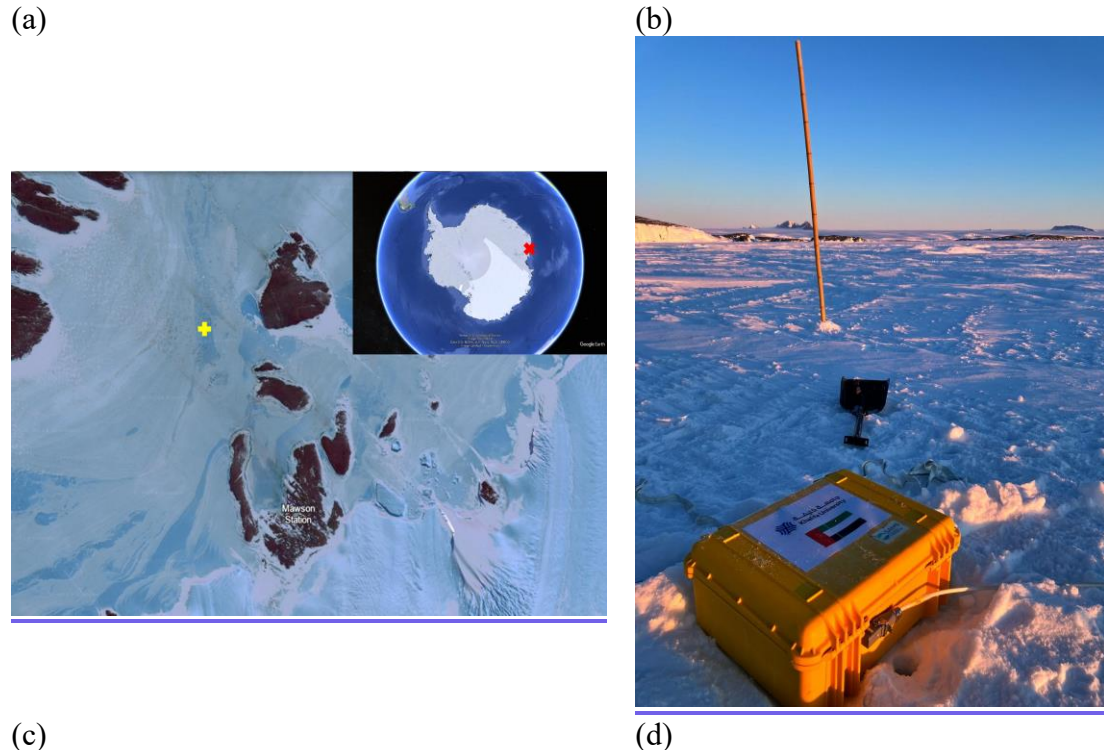
184 This paper is structured as follows. The observational datasets and model outputs and products
185 considered, and analysis techniques used, are described in Section 2. The measurements of SIT
186 and ST, including their variability and the mechanisms behind them, are discussed in Section 3.
187 Section 4 provides a case-study analysis of the period 11-16 July 2022, while in Section 5 the main
188 findings of the work are outlined and discussed.

189 **2. Methodology & Diagnostics**

190 **2.1. In-Situ Measurements at Khalifa SIMBA site off Mawson Station**

191 *In-situ* measurements of SIT and ST are obtained using a sea-ice mass-balance (SIMBA) unit
192 (Jackson et al., 2013). This SIMBA is deployed on landfast ice offshore from Mawson Station at
193 67.5912°S, 62.8563°E (Fig. 4e1a) on 7 July 2022, and remained *in-situ* until 7 December 2022.
194 The SIMBA unit, [Fig. 1b](#), consists of a 5 m-long thermistor string with a 0.02 m sensor spacing, a
195 barometer for surface air pressure, and an external sensor for near-surface ambient air temperature
196 (Jackson et al., 2013). During deployment, manual measurements of SIT and ST, as well as
197 freeboard, are recorded. The positions of the sensors relative to the interfaces are noted to establish
198 the initial state (on 7 July 2022). The measured SIT upon deployment is 0.988 m, the ST on top of
199 the sea ice is 0.156 m, and the sea-ice freeboard is 0.046 m. No manual validation or calibration is
200 conducted during the measurement period of 7 July - 7 December 2022.

201



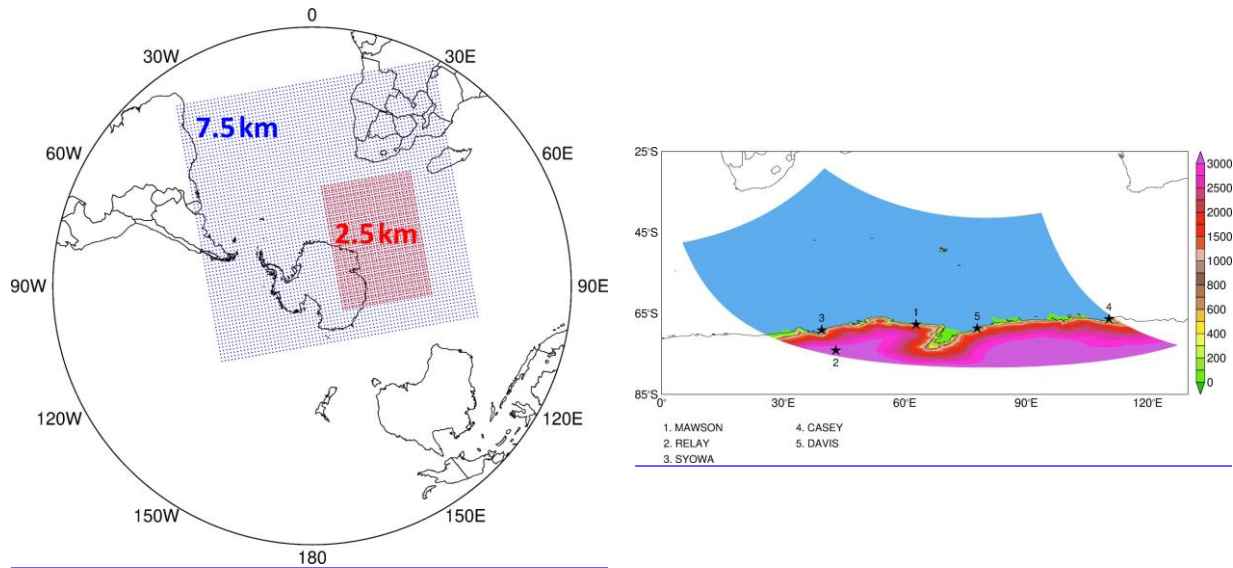


Figure 1: SIMBA Deployment Site and PolarWRF Simulation: (a) Spatial extent of the 7.5 km (blue) and 2.5 km (red) PWRF grids used in the numerical simulations. (b) Spatial extent and orography (m) of the 2.5 km PWRF grid. The stars highlight the location of the five weather stations considered in this work. (c) SIMBA deployment site (yellow cross) on the fast ice about 1.8 km off Mawson Station. Image source: Landsat 8 acquired on 19 November 2022. The red cross in the inset image, taken from Google Earth Pro, shows where Mawson Station is located in Antarctica. (d) SIMBA instrument prior to deployment. Image credit: Peter Caithness. (e) Spatial extent of the 7.5 km (blue) and 2.5 km (red) PWRF grids used in the numerical simulations. (f) Spatial extent and orography (m) of the 2.5 km PWRF grid. The stars highlight the location of the five weather stations considered in this work

202

203 The accuracy of the bus-addressable digital temperature sensing integrated circuit is ± 0.0625 K. A
 204 resistor is mounted directly underneath each thermistor sensor. A low voltage power supply (8 V)
 205 is connected to each sensor, to gently heat the sensor and its immediate surroundings. In this study,
 206 heating is applied to the sensor chain for durations of 30 s and 120 s once per day, with four vertical
 207 temperature profiles without heating also recorded daily. In this study, SIMBA data from 8 July to
 208 30 November 2022 are used to assess the evolution of SIT and ST at the site. The measurements
 209 are shown in Fig. 2. For the sensors 6 through 126, the actual temperature and the temperature rise
 210 after 120 s heating are given in Fig. 2a and 2b, respectively, with Fig. 2c showing the difference
 211 between the measurements of two adjacent temperature sensors after applying the heating.
 212

213 The vertical temperature gradients in the air above the surface and in the water below the ice
 214 bottom are generally very small (Jackson et al., 2013; Hoppmann et al., 2015; Liao et al., 2018).
 215 After 120 s of heating, the rise in temperature is approximately 10 times higher in air than in ice
 216 and water (Jackson et al., 2013). For any two adjacent sensors in the ice, and following the
 217 algorithm detailed in Liao et al. (2018) based on a physical model applied to the SIMBA
 218 measurements, the temperature difference should be ≤ 0.1875 K, whereas for two adjacent sensors
 219 in snow, the temperature difference should be ≥ 0.4375 K. These thresholds are applied to the
 220 temperature differences between adjacent sensors in the heating profile to identify the air-snow

221 and snow-ice interfaces (Jackson et al., 2013; Hoppmann et al., 2015; Liao et al., 2018). The ice-
 222 water interface is identified using a statistical approach based on Liao et al. (2018). A section of
 223 the thermistor string, spanning from the top of the sea ice to a few sensors below the water, is
 224 selected. The seawater temperature near the ice bottom remains stable around the freezing point
 225 (T_f). The temperature readings from this section are analyzed as a time series, and the most frequent
 226 value is identified as T_f . Scanning from bottom up, the last sensor close to T_f is identified as the
 227 ice bottom. The allowed temperature difference is 1.5 times the thermistor resolution of 0.0625 K.
 228 The temporal evolutions of the three interface locations are plotted in Figs. 2a-c.

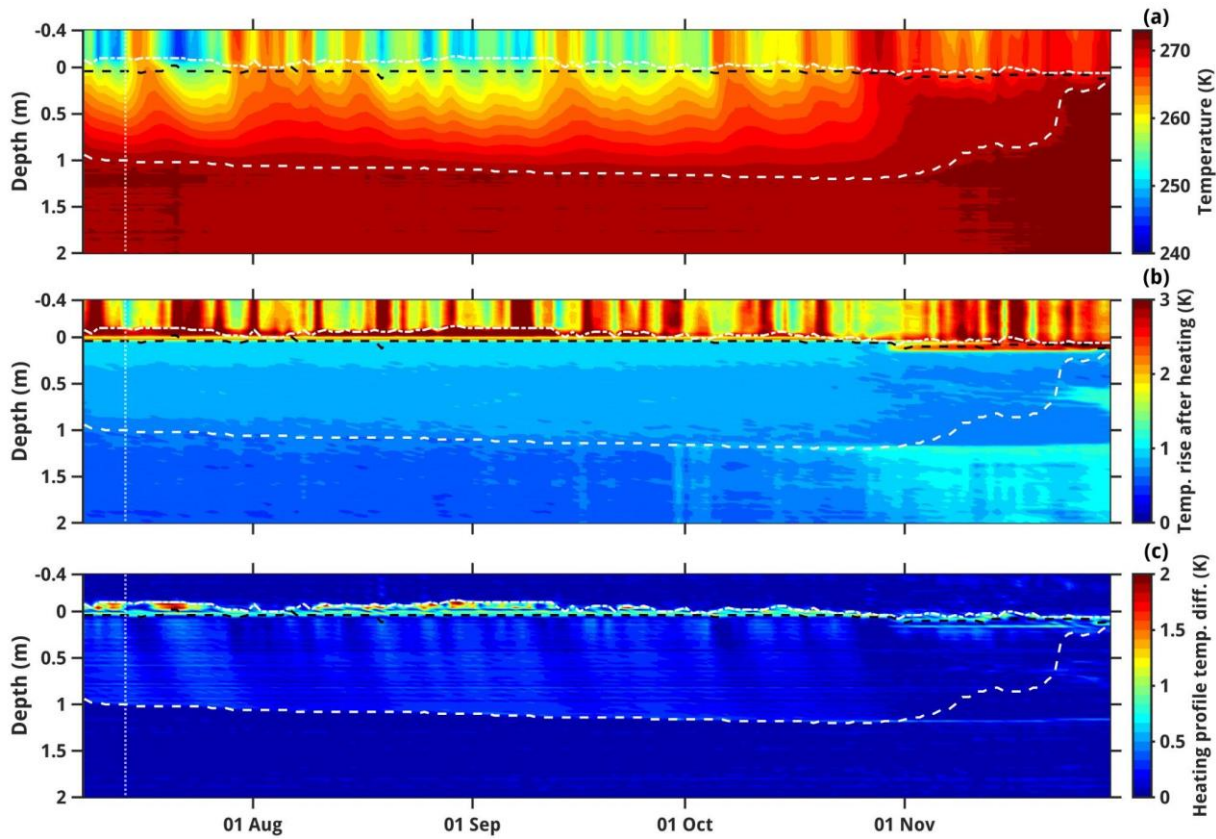


Figure 2: SIMBA measurements: (a) Temperature (K) evolution from the top of the chain through the ice down into the water (the zero line on the y-axis is at the snow-ice interface). (b) Temperature rise (K) after heating for 120 s. (c) Temperature difference (K) between adjacent sensors after applying the heating for 120 s. The vertical white dotted line indicates the day of AR occurrence at the site, 14 July. The horizontal dotted white line, black dashed line, and white dashed line give the air-snow (AS), snow-ice (SI), and ice-water (IW) interfaces, respectively.

229

230 **2.2. Observational and Reanalysis Datasets**

231 In addition to *in-situ* SIT and ST measurements, three observational datasets are considered in
 232 this work: (i) satellite-derived SIE and sea-ice velocity; (ii) ground-based observations at five
 233 weather stations, namely Mawson, Syowa, Relay, Casey, and Davis (Fig. 4b1d); and (iii) twice
 234 daily sounding profiles at the Mawson, Syowa, Casey, and Davis stations (stations #1 and 3-5 in
 235 Fig. 4b1d). Data from the fifth generation of the European Centre for Medium Range Weather
 236 Forecasting reanalysis (ERA-5; Hersbach et al., 2020) are used to investigate the large-scale
 237 circulation and SMB during the study period. ERA-5 is regarded as one of the best reanalysis
 238 products currently available over Antarctica and the Southern Ocean (Gossart et al., 2019; Dong
 239 et al., 2020). All of these products are listed in Table 1.

Dataset	Specifications
In-situ Sea-Ice Thickness and Snow Thickness	SIT and ST measurements just offshore of Mawson Station (67.5912°S, 62.8563°E) using a SIMBA unit; data available from 7 July to 7 December 2022
Sea-Ice Extent	Satellite-derived daily SIE at 3.125 km resolution; data available from June 2002 - Present
Sea-Ice Velocity	Satellite-derived daily sea-ice velocity at 62.5 km resolution; data available from December 2009 - Present
Weather Station Data	Ground-based observations at Mawson (67.6017°S, 62.8753°E; January 1954 - Present), Relay (74.017°S, 43.062°E; November 2021 - Present), Syowa (69.0053°S, 39.5811°E; January 1994 - Present), Casey (66.2825°S, 110.5231°E; February 1989 - Present), and Davis (68.5744°S, 77.9672°E; January 1957 - Present) Stations
Sounding Profiles	Twice daily at Mawson (67.6017°S, 62.8753°E; January 1954 - Present), Syowa (69.0053°S, 39.5811°E; January 2021 - Present), Casey (66.2825°S, 110.5231°E; February 1989 - Present), and Davis (68.5744°S, 77.9672°E; January 1957 - Present) Stations
ERA-5 reanalysis	Hourly products at $0.25^\circ \times 0.25^\circ$ (~27 km) spatial resolution; available from January 1940 - Present

241
 242 **Table 1: Observational and Reanalysis Datasets:** List of observational and reanalysis datasets used in
 243 this study.

244
 245 Daily SIE is derived from the measurements of sea-ice concentration collected by the
 246 Advanced Microwave Scanning Radiometer for Earth Observing Systems (AMSR-E) onboard the
 247 National Aeronautics and Space Administration (NASA) Aqua satellite from June 2002 to October

248 2011, and from the observations taken by the AMSR2 onboard Japan Aerospace and Exploration
249 Agency's Global Change Observation Mission - Water (GCOM-W) satellite from July 2012 to
250 present (Spreen et al., 2008). Sea-ice velocity vectors, on the other hand, are obtained from the
251 measurements collected by the Special Sensor Microwave Imager/Sounder onboard the United
252 States Air Force Defense Meteorological Satellite Program, the Advanced Scatterometer onboard
253 the European Space Agency's Meteorological Operational satellite, and the GCOM-W AMSR2
254 (Lavergne et al., 2010). Both the SIE and sea-ice velocity products are used to gain insight into
255 the effects of the warm and moist air intrusions on the sea-ice state around Mawson Station, as
256 performed in previous studies for other parts of Antarctica (e.g., Francis et al., 2021; Fonseca et
257 al., 2023).
258 .

259 *In-situ* observations at multiple Automatic Weather Stations (AWSs) are used in the analysis
260 and model evaluation (Fig. 4b1d). These include: (i) 1-minute 2-m air temperature and humidity,
261 10-m horizontal wind velocity, and sea-level pressure (SLP) observations at the Australian
262 Antarctic stations of Mawson, Casey, and Davis; (ii) 1-minute measurements of meteorological
263 parameters (2-m air temperature, SLP, 10-m horizontal wind velocity, and 2-m relative humidity)
264 and radiation fluxes (surface upward and downward and shortwave and longwave) at the coastal
265 Syowa Station; and (iii) 10-minute SLP, horizontal wind velocity, and 2-m air temperature and
266 relative humidity observations at the inland Relay Station. Also analyzed are data from
267 atmospheric sounding profiles acquired twice daily (at 00 and 12 UTC) at the Mawson, Syowa,
268 Casey, and Davis stations.

269 2.3. Numerical Models

270 Here we use version 4.3.3 of the Polar PWRF (Weather Research and Forecasting) model, a
271 version of the WRF model (Skamarock et al., 2019) optimized for the polar regions (Bromwich et
272 al., 2013; Hines et al., 2021; Xue et al., 2022; Zou et al., 2023), to simulate and investigate the AR
273 that impacted the Mac Robertson Land region on 14 July 2022. The model is run in a nested
274 configuration, with a 7.5km horizontal resolution grid domain comprising Antarctica, the Southern
275 Atlantic Ocean, southern Africa and the southwestern Indian Ocean, and a 2.5 km horizontal
276 resolution grid domain extending from the Southern Ocean just south of South Africa around 30°E
277 into coastal East Antarctica as far east as approximately 120°E (Fig. 4a1c). The choice of
278 resolution, in particular the 2.5 km grid that covers the bulk of the AR and associated warm and
279 moist air intrusion into East Antarctica, reflects the findings of Box et al. (2023) and Francis et al.
280 (2024). These studies stressed the need to properly resolve the fine-scale structure of an AR due
281 to the possible presence of AR rapid-like features embedded in the convective region, which can
282 generate copious amounts of precipitation and hence have a substantial impact on the SMB of the
283 ice. AR rapids are narrow (5-15 km wide), elongated (100-200 km long) and shallow (\sim 3 km deep)
284 linear features within the AR that propagate at high speed ($>30 \text{ m s}^{-1}$) and last for more than 24 h.
285 They have been reported for an AR that impacted Greenland in September 2017 (Box et al., 2023)
286 and another that wreaked havoc in the Middle East in April 2023 (Francis et al., 2024). AR rapids

287 are distinct from mesoscale convective systems (MCSs; Houze, 2004; Feng et al., 2021; Nelli et
288 al., 2021), which propagate at a slower speed ($10\text{-}20\text{ m s}^{-1}$), typically do not last as long (6-10 h),
289 and generate broader (as opposed to linear) precipitation structures.

290
291 PWRF is run from 10 July 2022 at 00 UTC to 17 July 2022 at 00 UTC, comprising the only AR
292 that impacted the site during July-November 2022, with the first day regarded as spin-up and the
293 output discarded. The hourly outputs of the 7.5 km and 2.5 km grids are used for analysis. The
294 physics schemes selected, listed in Table 2, reflect the optimal model configuration for Antarctica
295 and the Southern Ocean (Zou et al. 2021a, 2021b, 2023). In order to prevent the large-scales in the
296 model from drifting from the forcing fields, spectral nudging (Attada et al., 2021) is employed in
297 both grids for spatial scales $\gtrsim 1,000\text{ km}$ above $\sim 800\text{ hPa}$ and excluding the boundary layer. Fields
298 nudged include the horizontal wind components, the potential temperature perturbation, and the
299 geopotential height. In the vertical, 60 levels are considered, with the lowest level above the surface
300 at $\sim 27\text{ m}$ and roughly 20 levels in the range of $\sim 1\text{-}6\text{ km}$. The higher resolution in the low- to mid-
301 troposphere is crucial to correctly representing the fine-scale variability of the warm and moist air
302 masses impacting the site, and associated cloud processes (Rauber et al., 2020; Finlon et al., 2020).
303

Physics Scheme	Option Selected
Cloud Microphysics	Two-moment Morrison-Milbrandt P3 (Morrison and Milbrandt, 2015), with Vignon adjustment to improve the simulation of mid-level mixed-phase clouds over the Southern Ocean (Hines et al., 2021; Vignon et al., 2021)
Planetary Boundary Layer	Mellor-Yamada-Nakanishi-Niino level 1.5 (MYNN; Nakanishi and Niino, 2006)
Radiation	Rapid Radiative Transfer Model for Global Circulation Models (Iacono et al., 2008) for shortwave and longwave radiation
Cumulus	Kain-Fritsch (Kain, 2004) with subgrid-scale cloud feedbacks to radiation (Alapaty et al., 2012) only in 7.5 km grid
Land Surface Model (LSM)	Noah LSM (Chen and Dudhia, 2001; Tewari et al., 2004)
Sea Surface Temperature (SST)	6-hourly ERA-5 SSTs + Zeng and Beljaars (2005) surface skin temperature scheme

304
305 **Table 2: WRF Experimental Setup:** Physics scheme used in the WRF simulation.
306

307 PWRF is driven by 6-h ERA-5 data, with the SSTs and SIE used in the simulations taken from
308 ERA-5. Due to the lack of availability of SIT in ERA-5, the model's default SIT value of 3 m is

309 used in all sea-ice covered grid-boxes. The sea-ice albedo is parameterized as a function of air and
310 skin temperature following Mills (2011), with the model explicitly predicting ST on sea ice. A
311 sensitivity experiment is performed in which a more realistic representation of SIE and SIT is
312 considered. In particular, satellite-derived values are used for SIE, extracted from the 3.125 km-
313 resolution daily product available at the University of Bremen website (UoB, 2024), while the SIT
314 estimates at Mawson are employed at all sea-ice covered pixels. A similar model performance is
315 obtained with respect to the *in-situ* observations (not shown). Therefore, and for consistency with
316 the atmospheric forcing, the ERA-5's SIE and the PWRF's default SIT values are used in the
317 model runs.

318

319 The moisture sources that contributed to the AR during 11-16 July 2022 are diagnosed based
320 on 96-h back-trajectories obtained with the Hybrid Single-Particle Lagrangian Integrated
321 Trajectory (HYSPLIT; Stein et al., 2015) model driven by ERA-5 reanalysis data.

322 2.4. Diagnostics and Metrics

323 The performance of the PWRF model is assessed with the verification diagnostics proposed
324 by Koh et al. (2012) outlined in Supplement Section S1. In addition to the model bias, the two key
325 skill scores are (1) the normalized bias μ , defined as the ratio of the bias to the standard deviation
326 of the discrepancy between the model forecasts and observations; and (2) the normalized error
327 variance α , which accounts for both phase and amplitude errors. When $|\mu| < 0.5$ the model biases
328 can be regarded as not significant, while when $\alpha < 1$, the model forecasts are deemed to be
329 practically useful.

330 ARs are identified based on the Integrated Vapour Transport (IVT; $\text{kg m}^{-1} \text{s}^{-1}$), which is the
331 column integral of the water-vapour flux advected by the horizontal wind. It is quantified as

$$332 \quad IVT = \sqrt{\left(\frac{1}{g} \int_{1000 \text{ hPa}}^{200 \text{ hPa}} qu \, dp\right)^2 + \left(\frac{1}{g} \int_{1000 \text{ hPa}}^{200 \text{ hPa}} qv \, dp\right)^2} \quad (1)$$

333 In equation (1), g is the gravitational acceleration (9.80665 m s^{-2}), q is the specific humidity (kg
334 kg^{-1}), u is the zonal wind speed (m s^{-1}), v is the meridional wind speed (m s^{-1}), and dp is the
335 pressure difference between adjacent vertical levels (hPa). The criteria of Wille et al. (2021)
336 applied to ERA-5 data are used here to identify ARs. In particular, IVT has to exceed the 98th
337 percentile extracted for 1979-2022 at a given grid-box, and a minimum latitudinal extent of 20° is
338 required for the feature to be considered an AR. During the July to November 2022 study period,
339 the Khalifa SIMBA site on fast ice off Mawson Station is affected by one AR, on 14 July. This
340 event is selected for more in-depth analysis and modeling in Section 4. Large-scale circulation
341 patterns that favour ARs, including the presence of blocking and interaction with tropopause polar
342 vortices (TPVs), are also explored. Further details regarding the metrics used to diagnose them are
343 given in Supplementary Sections S2-S3.

344

345 The extratropical circulation can be modulated by tropical forcing, such as thermal (heating
 346 and cooling) anomalies (Hoskins and Karoly, 1981; Hoskins et al., 2012). In order to explore
 347 whether this occurs during the case study, the stationary wave activity flux that indicates the
 348 direction of the anomalous stationary Rossby wave propagation, defined in Takaya and Nakamura
 349 (2001), is derived equations (2a-b) and plotted.

$$350 \quad W_X = \frac{p \cos(\phi)}{2|u|} \left\{ \frac{u}{a^2 \cos(\phi)^2} \left[\left(\frac{\partial \psi'}{\partial \lambda} \right)^2 - \psi' \frac{\partial^2 \psi'}{\partial \lambda^2} \right] + \frac{v}{a^2 \cos(\phi)} \left[\frac{\partial \psi'}{\partial \lambda} \frac{\partial \psi'}{\partial \phi} - \psi' \frac{\partial^2 \psi'}{\partial \lambda \partial \phi} \right] \right\} \quad (2a)$$

351

$$352 \quad W_Y = \frac{p \cos(\phi)}{2|u|} \left\{ \frac{u}{a^2 \cos(\phi)} \left[\frac{\partial \psi'}{\partial \lambda} \frac{\partial \psi'}{\partial \phi} - \psi' \frac{\partial^2 \psi'}{\partial \lambda \partial \phi} \right] + \frac{v}{a^2} \left[\left(\frac{\partial \psi'}{\partial \phi} \right)^2 - \psi' \frac{\partial^2 \psi'}{\partial \phi^2} \right] \right\} \quad (2b)$$

353 In equations (2a-b), p is the ratio of the pressure level at which the W-vector is computed and
 354 1000 hPa, ϕ is the latitude, λ is the longitude, u and v are the zonal and meridional climatological
 355 wind speeds, respectively, $|u|$ is the climatological mean wind speed, and ψ' is the streamfunction
 356 anomaly.

357

358 Variability in the ST, and perhaps to a lesser extent the SIT, is directly related to the SMB,
 359 which can be expressed as

$$360 \quad SMB = P - Q_{sfc} - M - Q_{snow} - D \quad (3)$$

361 where P is the precipitation rate (mostly snowfall), Q_{sfc} is the surface evaporation/sublimation
 362 rate, M is the surface melt and runoff rate, Q_{snow} is the blowing snow sublimation rate, and D is
 363 the blowing snow divergence rate term, all with units of mm w.e. hr^{-1} . Blowing snow refers to
 364 unconsolidated snow moved horizontally across the ice surface by winds above a certain threshold
 365 speed (Massom et al., 2001). As detailed in Francis et al. (2023), the P and M terms are directly
 366 extracted from ERA-5, for which the reanalysis values are in close agreement with satellite-derived
 367 estimates over Antarctica, while the remaining three (Q_{sfc} , Q_{snow} , D) are calculated using
 368 parameterization schemes, described in Supplement Section S4. The hourly PWRF output is also
 369 used to estimate the SMB for the 11-16 July 2022 case study, with M given by the decrease in ST
 370 when the air temperature is above freezing after accounting for the other processes. Positive values
 371 of SMB indicate an accumulation of snowfall at the site, while negative values represent a
 372 reduction due to melting, sublimation or wind erosion processes, or a combination of the three. It
 373 is also important to note that, following the convention of Dery and Yau (2002) adopted by Francis
 374 et al. (2023), positive values of Q_{sfc} indicate deposition while negative values indicate
 375 sublimation. For Q_{snow} , on the other hand, positive values indicate sublimation and negative
 376 values indicate deposition.

377

378 Foehn effects, which play an important role in the SMB (e.g., Kuipers Munneke et al., 2017;
 379 Francis et al., 2023), are identified using the methodology proposed by Francis et al. (2023). If, at
 380 a given grid-point and hourly timestamp, the 2-m temperature exceeds its 60th percentile, the 2-m

381 relative humidity drops below its 30th percentile, and the 10-m wind speed exceeds its 60th
382 percentile, Foehn effects occur. The percentiles are grid-point dependent and are extracted for the
383 period 1979-2021. Monthly hourly thresholds are used for the 2-m temperature to account for the
384 annual cycle, while for the relative humidity and wind speed they are extracted for the full period.

385 3. Sea-Ice and Snow Thickness Variability

386 In Figs. 3ea-fb, the derived values of ST and SIT from 8 July to 30 November 2022 at the
387 Khalifa SIMBA site on fast ice off Mawson Station are plotted. The uncertainty, which is estimated
388 to be 7% for ST and 2% for SIT (Liao et al., 2018), is highlighted by the blue shading. The SIT
389 exhibits a gradual increase starting on 8 July, peaking at 1.14-1.16 m from 19-24 October, followed
390 by a steady decline to 0.06-0.10 m at the end of November. These values are comparable to those
391 estimated for this region and time of year using satellite-derived products, which are typically in
392 the range 0.50-1.50 m (Kacimi and Kwok, 2020). The ST on top of the ice, on the other hand,
393 exhibits pronounced day-to-day variations as high as 0.08 m, peaking in mid-August to early
394 September, and with values not exceeding 0.10 m from mid-September to the end of November.
395 These values are also in the range of those derived from satellite altimeter data for that coastal
396 region (Kacimi and Kwok, 2020).

397

398 In order to explore whether atmospheric forcing could have played a role in the observed
399 variability in SIT and ST, the local SMB is estimated around the Khalifa SIMBA site on fast ice
400 off Mawson Station using ERA-5 data (Figs. 3c-d). An analysis of Figs. 2 and 3 reveals that the
401 SIT appears to be mostly driven by the growth (increase in SIT) and melting (decrease in SIT) at
402 the ice bottom which, on top of the oceanic heat flux (Heil et al., 1996; Haas, 2017), depends on
403 the conductive heat flux driven by the atmospheric forcing. The annual SIT decrease that initiates
404 in late October coincides with the time when the air temperature climbs above 265 K (Fig. 2a; Fig.
405 3e3e) and there is increased solar insolation (note the strong diurnal variation in air temperature in
406 Fig. 3e3e) at the site. On the other hand, a comparison of the ST observations and the SMB
407 estimated from ERA-5 (equation 3) reveals a good correspondence between the two (cf. Figs.
408 3a3b-b with 3e3c-d). In particular, instances of positive SMB values (based on ERA-5) are
409 typically associated with and followed by an increase in the measured ST at the site (e.g., in early
410 July, mid-August, early and mid-October and mid-November), while negative SMB values from
411 ERA-5 are accompanied by a decrease in the observed ST (e.g., in late July-early August and in
412 late September-early October). Besides precipitation (snowfall) events, which can lead to an
413 increase in ST by up to 0.06 m, Foehn winds-effects also modulate the ST. These correspond to
414 episodes when the wind direction is offshore (typically southerly to southeasterly), with an
415 increase in wind speed and air temperature and a decrease in relative humidity. Foehn timestamps,
416 identified following the methodology proposed by Francis et al. (2023) described in section 2.4,
417 are shaded in purple in Fig. 3d. Several of these occurrences are seen during the study period, such
418 as in mid-July, early August, mid-September and late October, leading to a reduction in ST of up
419 to 0.08 m in a day (cf. Figs. 3e3b-ef). This is not surprising, as the Khalifa SIMBA site on fast ice

420 off Mawson Station is exposed to katabatic winds flowing seaward off the interior plateau (Dare
421 and Budd, 2001), which experience adiabatic compression as they descend towards coastal areas.
422 If the air temperature, relative humidity, and wind speed meet the criteria detailed in section 2.4,
423 Foehn effects occur. Blowing snow, albeit less frequently, also affects the variability of ST: e.g.,
424 at the beginning of August, there is a 0.08 m decrease in ST during a blowing snow sublimation
425 episode (Q_{snow} reaches 0.25 mm w.e. hr^{-1}) followed by a Foehn event (Figs. 3b-ef). Blowing snow
426 divergence, D , on the other hand, plays a much-reduced role in the SMB, being of a larger
427 magnitude during the passage of the AR on 14 July that brought wind speeds in excess of 30 m s^{-1}
428 (Figs. 3b-ef). Surface melting is unlikely to be a major driver of ST, as evidenced by the zero
429 values of M during the measurement period (Fig. 3b3d). This is because during July-November
430 2022, the surface and air temperatures at the site remained below freezing (Figs. 2a and 3e3e).
431

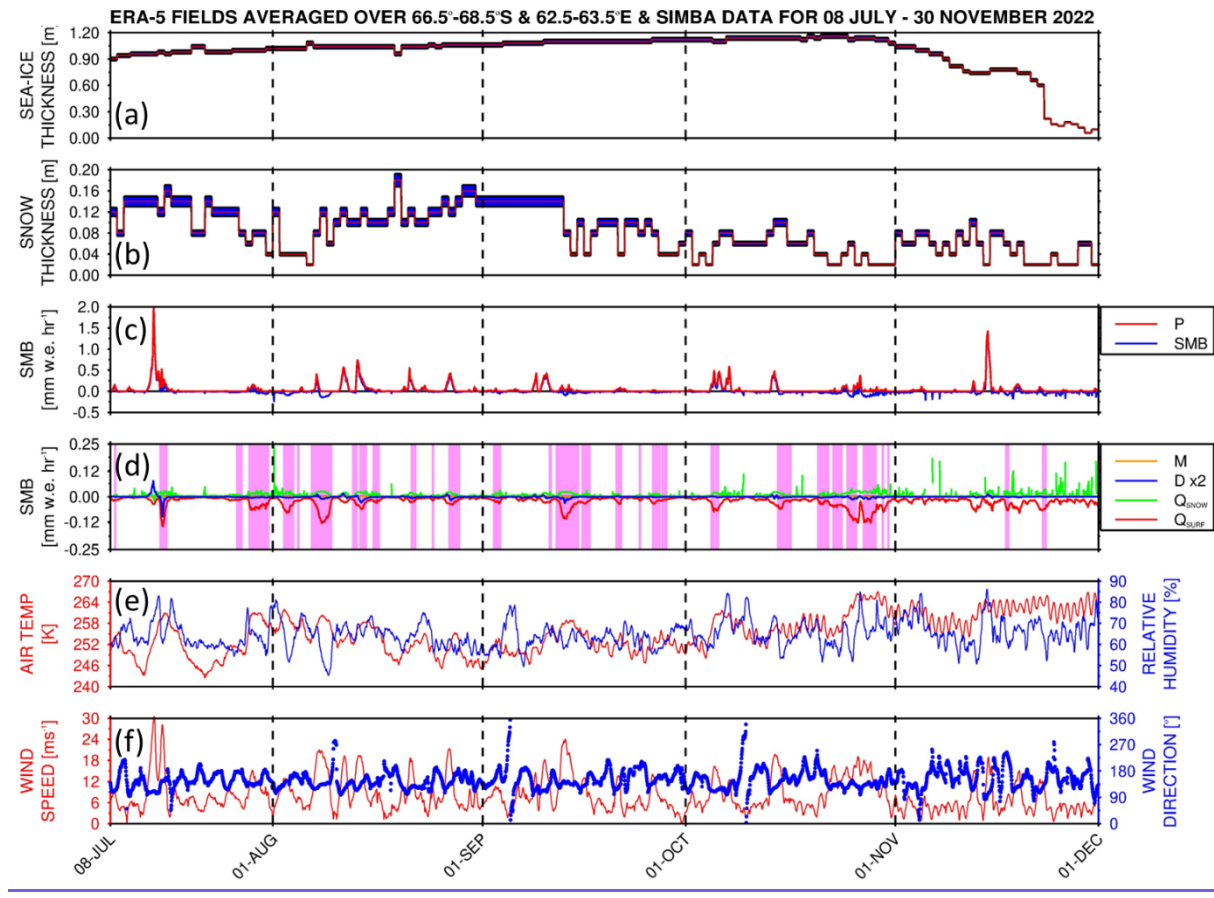
432 Figs. 3g-l zoom-in during 11-16 July, when an AR impacted the site. The 0.02 m variations in
433 SIT during 15-16 July, -(Fig. 3lg) are within the uncertainty range and hence can be ascribed to
434 the uncertainties in the methodology used for its estimation. The changes in ST, Fig. 3h, on the
435 other hand, can be linked to atmospheric forcing (cf. Figs. 3i-j). On 14 July, heavy precipitation
436 (>2 mm w.e. hr^{-1}) and strong easterly to southeasterly winds (>30 m s^{-1}) occurred in association
437 with the AR, with a steady increase in air temperature from around 245 K on 13 July to 256 K at
438 the beginning of 15 July (Figs. 3g and 3i-j3k-l). On the following day, Foehn effects occurred, Fig.
439 3j, as evidenced by in line with the decrease in relative humidity from ~83% to 60%, the increase
440 in wind speed from 12 to 28 m s^{-1} with a shift from an easterly (96°) to a southeasterly (156°)
441 direction, and a further 4 K increase in air temperature, Figs. 3k-li-j. The negative Q_{sfc} , which
442 indicates surface sublimation, plays the largest a major role in the SMB during Foehn periods, Figs.
443 3i-jg-h, in line with Francis et al. (2023). The 0.02 m drop in ST from 15 to 16 July, Fig. 3k3h, can
444 be attributed to Foehn effects, while the absence of an increase in ST during the AR may be
445 explained by the strong winds (Fig. 3l) that blow the snow away and prevent it from accumulating
446 at the instrument's location (note the positive blowing snow divergence, D , during the precipitation
447 event, Fig. 3h3i). In fact, it has been reported that strong katabatic winds have blown the snow
448 away as quickly as it falls on nearshore fast ice near the Mawson (Dare and Budd, 2001) and
449 Syowa (Kawamura et al., 1995) stations, resulting in very low accumulation close to the coast.
450 ERA-5 predicts some precipitation on 16 July, Fig. 3g3i, even though at much reduced levels
451 compared to 14 July. However, the fact that the wind speed is much lower on this day, dropping
452 below 2 m s^{-1} (Fig. 3j3l), allows for snow accumulation at the Khalifa SIMBA site on fast ice off
453 Mawson Station, which that contributes to the observed 0.04 m increase in ST. The 0.02 m
454 variations in SIT during 15-16 July (Fig. 3l) are within the uncertainty range and hence can be
455 ascribed to uncertainties in the methodology used for its estimation. It is important to note that a
456 longer measurement period that comprises multiple AR passages would be needed for a robust
457 link between ARs and their effects on ST and SIT to be established.
458

459 Figure 4a gives the Pook Blocking Index, defined in Equation S6, for the study period. It
460 reveals a few blocking events east of the site around 120°E in late July-early August, 150°E in mid-
461 September, and around the Dateline in mid- to late-November. Zoomed-in plots around the time
462 of the Mawson AR passage highlight the occurrence of blocking around the Dateline and 60°W
463 (Fig. 4d). The latter actually coincided with the passage of three consecutive ARs west of the
464 Antarctic Peninsula (Fig. 4f), with the air temperature climbing above freezing (Fig. 4e). Wille et
465 al. (2024c) and Maclennan et al. (2023) stressed that the occurrence of blocking can lead to the
466 development of an “AR family” (or multi-AR) event, with the counterclockwise flow around the
467 high-pressure and subsequent poleward advection of warm and moist low-latitude air masses
468 leading to a marked rise in temperature. This is evident in particular around 120°E in late July-
469 early August and mid-September, and around 150°E in late November (Figs. 4a-c). At the Khalifa
470 SIMBA site on fast ice off Mawson Station, on the other hand, blocking did not occur, as evidenced
471 by the small values of the Pook Blocking Index (Fig. 4a). During the case study in mid-July (Figs.
472 4d-f), the presence of a ridge east of Mawson led to a second warm and moist air intrusion around
473 70°-90°E on 16 July. The passage of the AR at Mawson on 14 July coincided with an increase in
474 air temperature by more than 15 K in a couple of days (Fig. 4e), consistent with the observed rise
475 in air temperature of ~18 K at the site (Fig. 2a).

476

477 The results in Figure 4 highlight the role of atmospheric dynamics in modulating the ST at the
478 Khalifa SIMBA site on fast ice off Mawson Station, with the SIT largely controlled by the oceanic
479 and conductive heat flux and the seasonal variability in the incoming solar radiation.

480



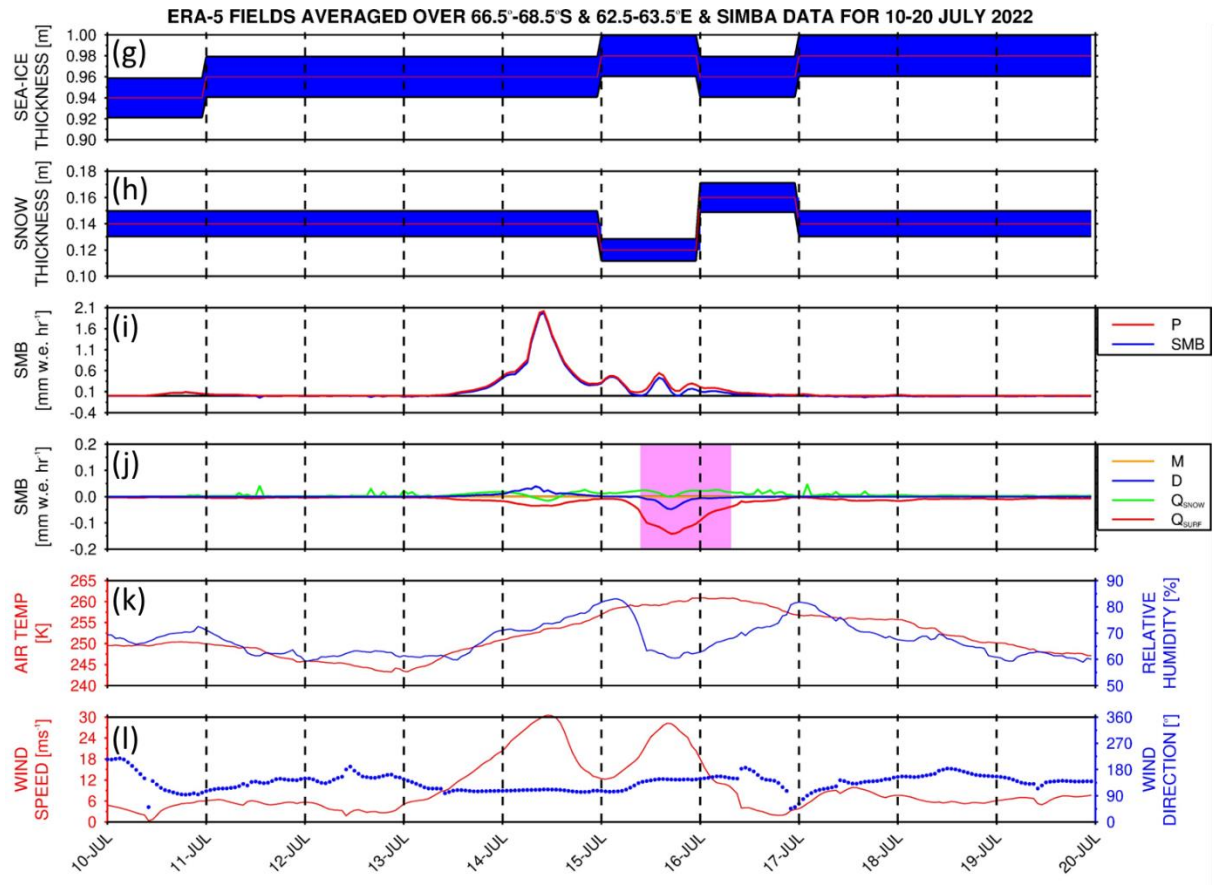


Figure 3: Surface Mass Balance and SIMBA Observations: (a) ST and (b) SIT from the SIMBA measurements for the period 08 July to 30 November 2022. The red line shows the observed values while the blue shading gives the uncertainty, which is estimated as 7% for ST and 2% for SIT (Liao et al., 2018). (c)-(d) give the hourly SMB terms (mm w.e. hr^{-1}) from ERA-5 averaged over the domain 66.5° - 68.5° S and 62.5° - 63.5° E. Shown is the SMB (blue) and precipitation (red; P) in (c), and the snowmelt (orange; M), surface sublimation (red; Q_{sfc}), blowing snow sublimation (green; Q_{snow}), and blowing snow divergence (blue; D) in (d). No snowmelt occurred during the measurement period, and the D term is multiplied by two for visualization purposes. The purple shading in (d) highlights hourly timestamps when Foehn effects occurred anywhere in the domain. (e)-(f) give the reanalysis' domain averaged ERA-5-hourly (a)-(b) surface mass balance (mm w.e. hr^{-1}), (e) air temperature (red; K) and relative humidity (blue; %) in (e), and (f) horizontal wind speed (red; m s^{-1}) and direction (blue; $^{\circ}$) in (f) averaged over 66.5° - 68.5° S and 62.5° - 63.5° E for the period 08 July and 30 November 2022. The local SMB terms plotted are the SMB (blue) and precipitation (red; P) in (a), and the snowmelt (orange; M), surface sublimation (red; Q_{sfc}), blowing snow sublimation (green; Q_{snow}), and blowing snow divergence (blue; D) in (b). No snowmelt occurred during the measurement period, and the D term is multiplied by two for visualization purposes. (e)-(f) give the ST (m) and SIT (m) from the SIMBA measurements, respectively. The red line shows the observed value while the blue shading gives the uncertainty, which is estimated as 7% for ST and 2% for SIT (Liao et al., 2018). (g)-(l) are as (a)-(f) but for 10-20 July 2022. No scaling is applied to the D term in (j).

481

482

483

484

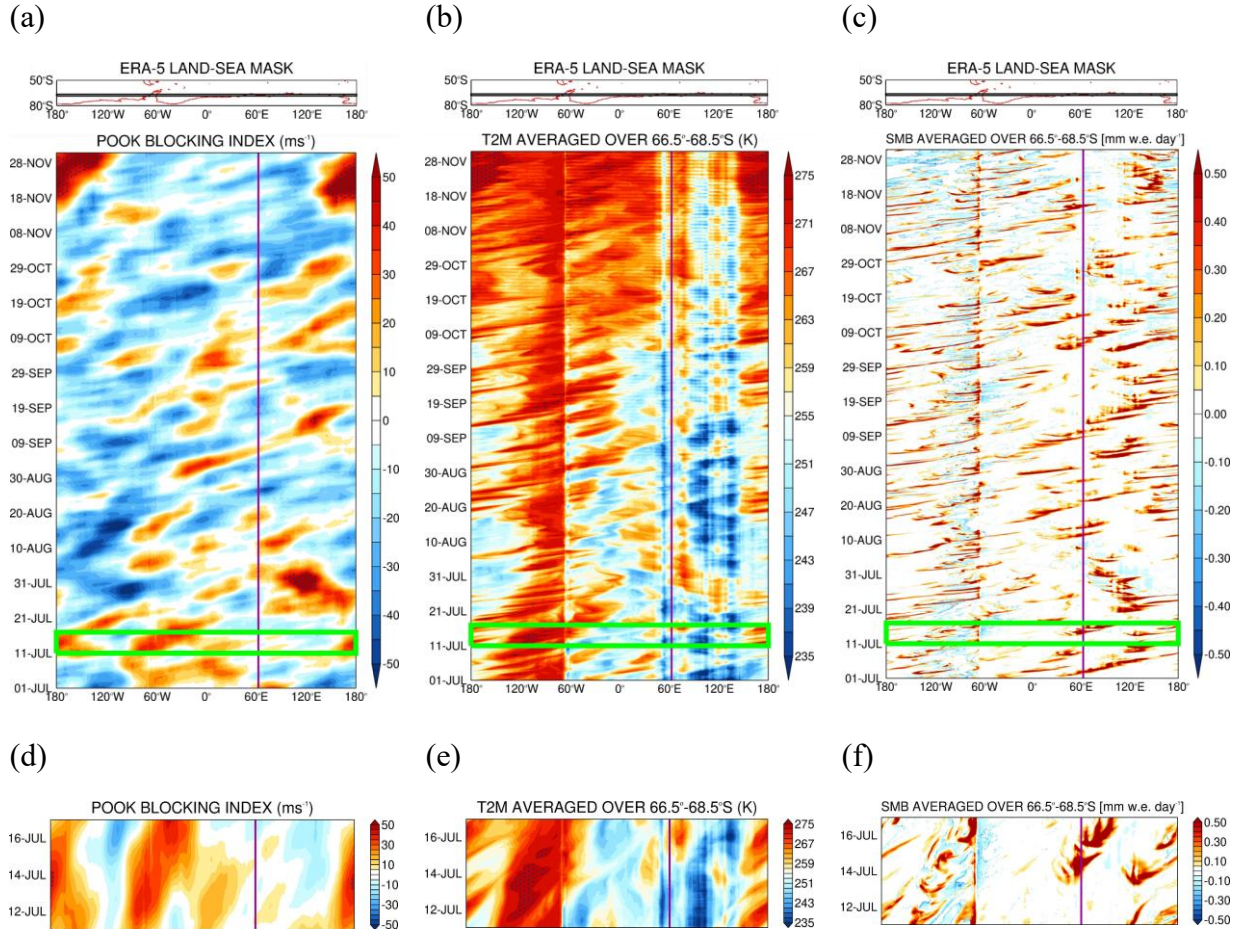


Figure 4: Atmospheric dynamics and thermodynamics during the Observational Period: (a) Pook blocking index (m s^{-1}) for July–November 2022. The vertical purple line gives the approximate longitude of the measuring site. Regions where the index exceeds 40 m s^{-1} , an indication of a high degree of blocking, are stippled. The green rectangles indicate the period when an AR impacted the site 11–16 July. Above the Hovmöller plot, the land-sea mask as seen by ERA-5 is plotted in red and the averaging region is highlighted with a black rectangle. (b) and (c) are as (a) but for air temperature (K) and the SMB, defined in equation (3), respectively, averaged over 68.5° – 66.5° S. The sharp transition in the temperature field around 60° W arises due to the presence of the Antarctic Peninsula (landmass), while the stipple in (b) indicates regions and times when the temperature is above freezing (273.15 K). (d)–(f) are as (a)–(c) but zooming in for 11–16 July 2022.

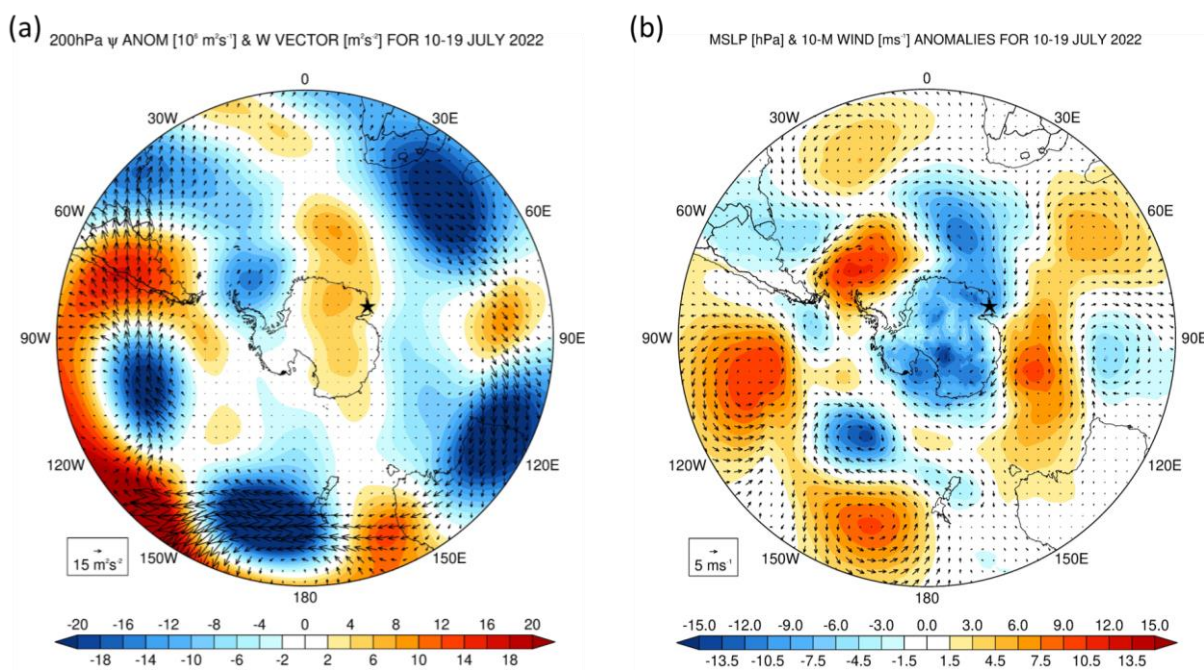
487 **4. Case Study: 11–16 July 2022**

488 An AR impacted the site during July–November 2022 on 14 July. In Section 4.1, the large- and
489 regional-scale environment that promoted the development of the AR is investigated, while in
490 Section 4.2 the results of the PWRF simulations are discussed.

491 **4.1 Large-Scale Atmospheric Patterns**

492 The period 10-19 July 2022 is characterized by a strong wavenumber 3 pattern along the
 493 Southern Hemisphere polar jet at about 60°S and a wavenumber 5 pattern along the subtropical jet
 494 at about 30°S (Fig. 5a), projecting onto the positive phase of SAM (Fig. 5b). The stationary wave
 495 activity flux vectors in Fig. 5a show little wave propagation from the tropics into the Southern
 496 Hemisphere mid-latitudes, with a prevailing zonal propagation within the wavenumber #5 pattern.
 497 This is also evidenced by the strong westerly flow around Antarctica (Fig. 5d). One of the reasons
 498 for the positive SAM is the La Niña that was taking place at the time, the third consecutive La
 499 Niña year after the 2018-2019 El Niño (NOAA/NWS, 2024), [as La Niña events typically project
 500 onto the positive SAM pattern \(Fogt et al., 2011\)](#).

501



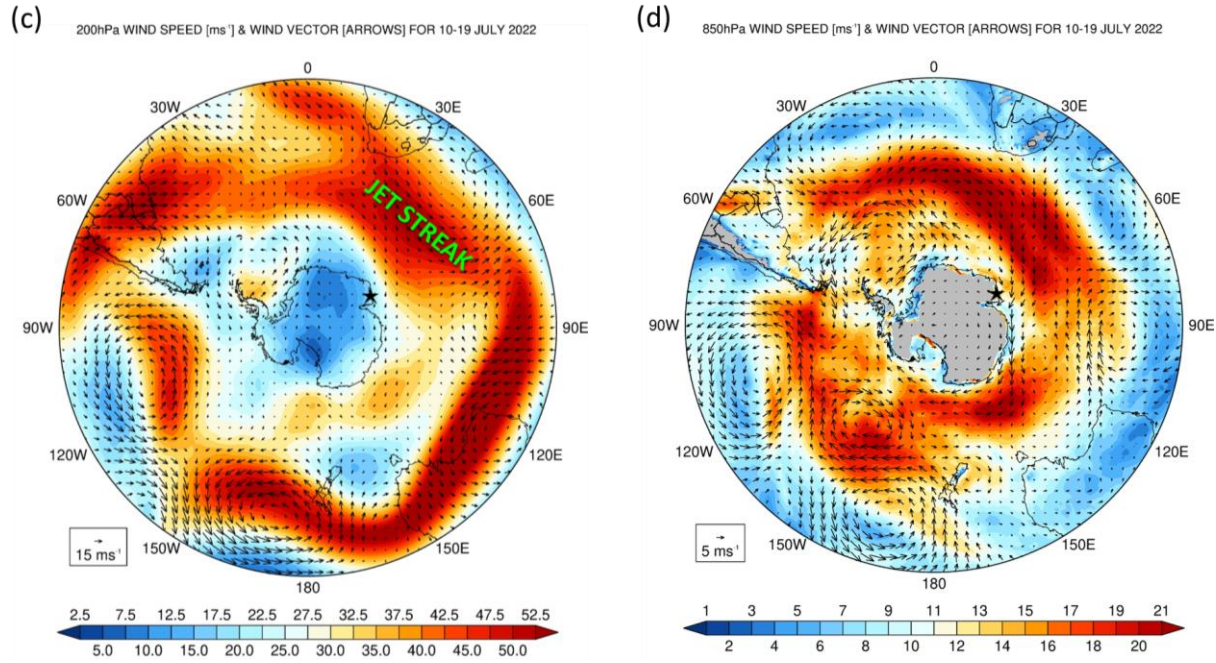


Figure 5: Large-Scale Circulation during 10-19 July 2022: (a) 200 hPa stream-function anomalies (shading; $10^6 \text{ m}^2 \text{s}^{-1}$), with respect to the hourly 1979-2021 climatology, and stationary W vectors (Takaya and Nakamura, 2001; equations (2a) and (2b); arrows; $\text{m}^2 \text{s}^{-2}$) averaged over 10-19 July 2022. (b) Sea-level pressure (shading; hPa) and 10-m wind vectors (arrows; m s^{-1}) anomalies for the same period. (c) and (d) show the 200 hPa and 850 hPa wind speed (shading; m s^{-1}) and vectors (arrows) averaged over the same period. The jet streak referred to in the text is highlighted in (c). In all panels, the star gives the location of Mawson Station (67.5912°S , 62.8563°E).

502

503

504 North of Mawson Station, a pressure dipole is present around 40° - 65°S (Fig. 5b), with a ridge to
 505 the east and a trough to the west. This pattern favours the poleward propagation of warm and moist
 506 low-latitude air into the Khalifa SIMBA site on fast ice off the Mawson Station in East Antarctica,
 507 and is conducive to the development of ARs (Francis et al., 2022b; Gorodetskaya et al., 2023).
 508 The interaction between the subtropical jet and polar jet led to the development of a jet streak (Fig.
 509 5c), a localized maximum in the strength of the flow. The low pressure associated with the AR
 510 (Fig. 5a) is located to the south of the jet entrance, in an area favourable for cyclogenesis (Wallace
 511 and Hobbs, 2006). Despite its slow eastward movement and anomalous high strength, the
 512 meridional extent of the ridge from East Antarctica to southeastern Madagascar may explain why
 513 it is not detected by the Pook Blocking Index, Fig. 4a and Equation S6, as the westerly flow at 35° -
 514 40°S and 65° - 70°S is also weaker. The AR that developed on 14 July 2022 is particularly
 515 remarkable, extending from the southwestern Indian Ocean into the Southern Ocean and East
 516 Antarctica, and having its primary origin in South America (Figs. 6a-b). The wavetrain extending
 517 from South America to the southeastern Pacific Ocean comprises a ridge over southern parts of
 518 Chile and Argentina, and a low over northern Argentina to the west of South Atlantic subtropical
 519 high (Figs. S1b, S1d and S1f). The pressure gradient between the latter two systems leads to a
 520 strengthening of the South American low-level jet (Marengo et al., 2004; Montini et al., 2019),

521 which advects moisture from equatorial South America into the subtropics and helps to feed
522 convection east of the Andes (Figs. S1a, S1c, and S1e). The moist outflow coming out of South
523 America and the latent heat release from the convection strengthen the low pressure to the
524 southwest of South Africa that is tracking southeastwards, and promote the development of the
525 AR that impacted the Khalifa SIMBA site on fast ice off Mawson Station on 14 July. After a first
526 landfall on 14 July around Mawson Station, Fig. 6a, the AR made a second landfall around 75°-
527 90°E, Fig. 6b, impacting a wide swath of East Antarctica from about 45°E to 100°E. Here, the air
528 temperature anomalies generally exceeded 10 K, with some parts of East Antarctica having near-
529 surface temperatures in the top 1% of the 1979-2021 climatological distribution (Fig. 6d). The IVT
530 at 06 UTC on 14 July exceeds $156 \text{ kg m}^{-1} \text{ s}^{-1}$ around the Khalifa SIMBA site on fast ice off Mawson
531 Station and $800 \text{ kg m}^{-1} \text{ s}^{-1}$ further north along the AR (Fig. 6b), with the hourly IVT on this day
532 being in the top 0.5% of the climatological distribution (Fig. 6c), an attestation to the extreme
533 nature of this event. A back-trajectory analysis performed with HYSPLIT forced with ERA-5 data
534 revealed tropical and subtropical moisture sources contributed to the 14 July 2022 AR (Fig. S2a).
535 While at lower levels the moisture came from the Southern Ocean, with specific humidity values
536 generally below 2 g kg^{-1} and air temperatures generally below freezing, at 2250 m it originated in
537 the subtropics just south of South Africa with specific humidity values in excess of 6 g kg^{-1} and
538 air temperatures around 280-290 K (Figs. S2b-e). The latter air mass ascended from roughly 200
539 m to 2250 m just north of Mawson Station, when it encountered the colder and drier [katabatic](#)
540 airflow (Fig. S2a). Several studies report on ARs impacting Antarctica being fed by subtropical
541 moisture, such as the February 2011 (Terpstra et al., 2021) and the November-December 2018
542 (Gorodetskaya et al., 2020) ARs over East Antarctica, and the February 2022 AR over the
543 Antarctica Peninsula (Gorodetskaya et al., 2023).
544

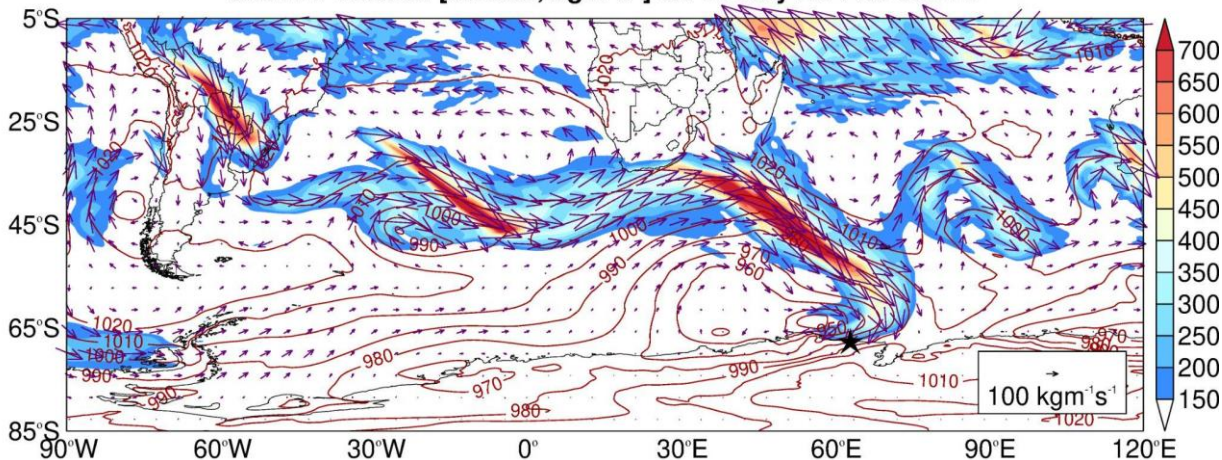
545 The AR and attendant cyclone also had an important effect on the sea ice in the region. As seen in
546 Figs. S3a-b, there was a considerable reduction in SIE from 12 to 16 July both around coastal
547 Antarctica and upstream, with an open-ocean polynya developing well northwest of Mawson
548 Station around $65^{\circ}\text{S}, 45^{\circ}\text{E}$ on 14 July and disappearing on 22 July. The role of ARs and the surface
549 divergent flow associated with the attendant cyclone in opening up polynyas has been reported at
550 multiple sites around Antarctica (Francis et al. 2019, 2020). The low-pressure system northwest of
551 Mawson reached a minimum value of 944 hPa on 12 July over the Southern Ocean, with the
552 secondary low that formed on 14 July reaching 933 hPa on this day at 06 UTC just off the Khalifa
553 SIMBA site on fast ice off Mawson Station (Fig. 6a), and deepening further to 931 hPa late on 15
554 July just to the northeast of the site (Fig. 6b). These systems are stronger than those that played a
555 role in the opening up of the Weddell Sea Polynya in September 1973 and 2017 (Francis et al.,
556 2020), and the Maud Rise Polynya in September 2017 (Francis et al., 2019). The sea-ice vectors
557 in Figs. S3c-d show an equatorward movement north of Mawson Station from 12-14 July (prior to
558 the event) at speeds in excess of 40 km day^{-1} , and a southward movement from 14-16 July (post
559 event) at speeds in excess of 20 km day^{-1} . These sea-ice drift velocities, which are associated with
560 the changing wind field in response to the shift in the position of the mid-latitude weather systems

561 in the region (Figs. 6a-b, 6d and 7) are higher than those observed in the western Ross Sea in late
 562 April 2017 (Fonseca et al., 2023), and comparable to those estimated in the region in September
 563 2017 (Francis et al., 2019).

564

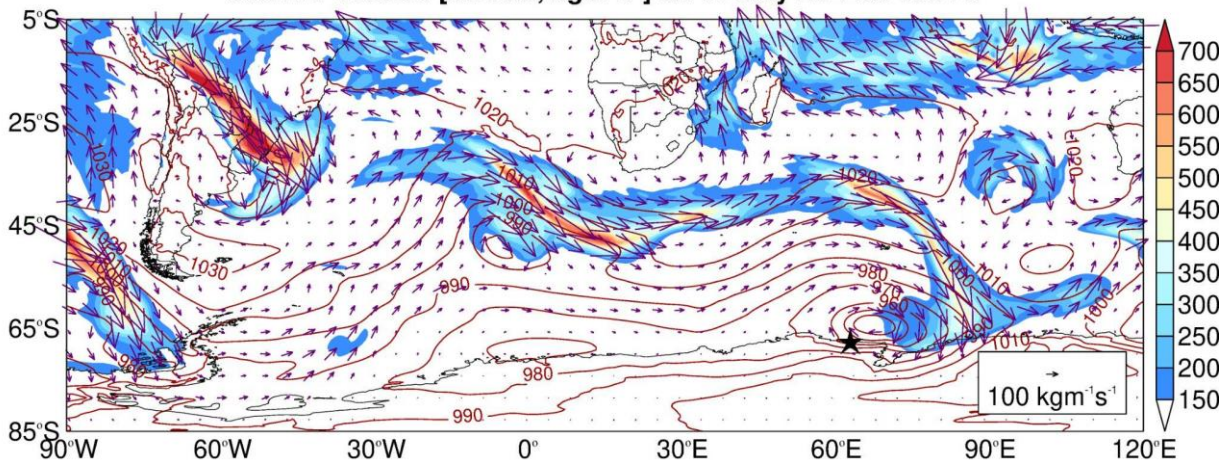
(a)

Sea-Level Pressure [contours; hPa], IVT Magnitude [shading; $\text{kgm}^{-1}\text{s}^{-1}$]
 and IVT Vectors [arrows; $\text{kgm}^{-1}\text{s}^{-1}$] on 14 July 2022 at 06UTC



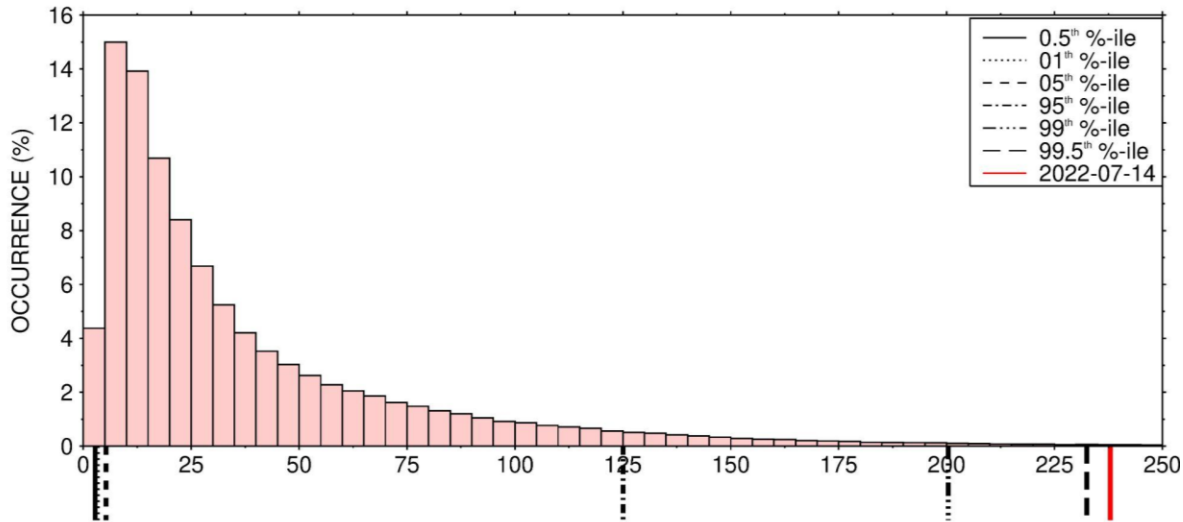
(b)

Sea-Level Pressure [contours; hPa], IVT Magnitude [shading; $\text{kgm}^{-1}\text{s}^{-1}$]
 and IVT Vectors [arrows; $\text{kgm}^{-1}\text{s}^{-1}$] on 15 July 2022 at 15UTC



(c)

MAXIMUM OF HOURLY IVT ($\text{kg m}^{-1} \text{s}^{-1}$) OVER 68.5°-66.5°S & 62.5°-63.5°E FOR 1979-2021



(d)

AIR TEMPERATURE [K] & 10-M WIND [ms^{-1}] ANOMALIES ON 16-JUL-2022 @ 00UTC
GREEN STIPPLE: AIR TEMPERATURE IN TOP 1% OF 1979-2021 CLIMATOLOGY

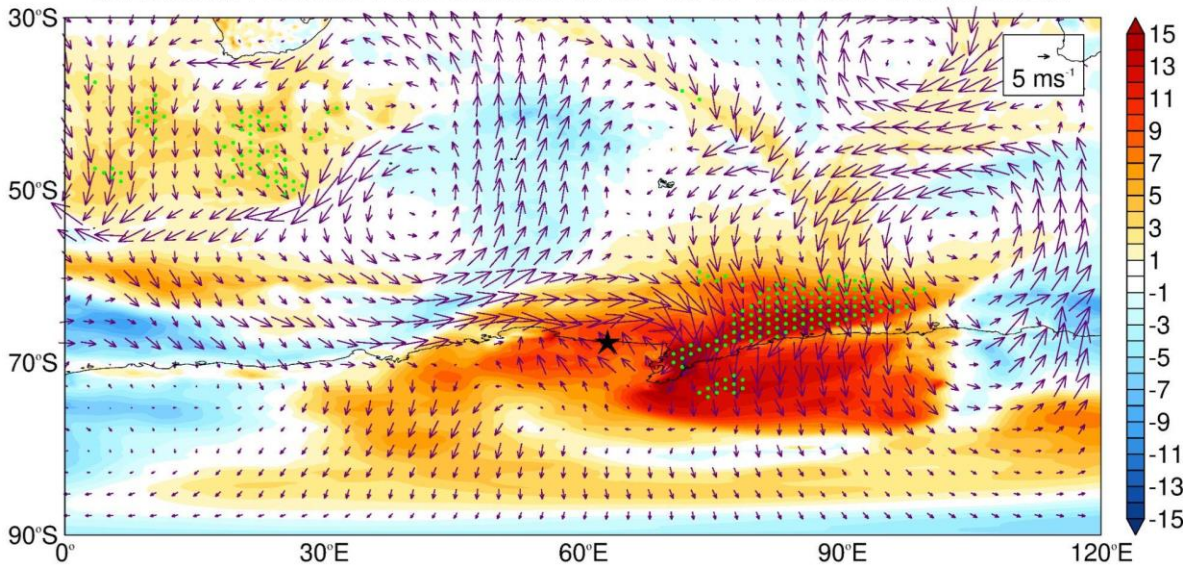


Figure 6: Atmospheric River on 14 July 2022: (a) Sea-level pressure (contours; every 10 hPa), Integrated Vapour Transport (IVT) magnitude (shading; $\text{kg m}^{-1} \text{s}^{-1}$) and vectors (arrows; $\text{kg m}^{-1} \text{s}^{-1}$) on (a) 14 July 2022 at 06 UTC and (b) 15 July 2022 at 15 UTC from ERA-5. The star gives the location of the Mawson station. (c) Histogram of the maximum hourly IVT around the Mawson station (68.5°-66.5°S and 62.5°-63.5°E) for 1979-2021. The solid, dotted, dashed, dotted-dashed, dashed-dotted-dotted and long dashed lines give the 0.5th, 1st, 5th, 95th, 99th and 99.5th percentiles, respectively, while the red line indicates the maximum hourly values on 14 July 2022. (d) air temperature (shading; K) and 10-m wind vectors (arrows; ms^{-1}) anomalies with respect to 1979-2021 climatology on 16 July 2022 at 00 UTC. The green stipple indicates regions where the air temperatures are in the top 1% of the 1979-2021 climatological distribution.

566 Figures 5-6 provide a summary of the weather conditions during 10-19 July 2022, with Fig. 6
567 focusing on the AR event that impacted Mawson Station on 14 July. In order to gain insight into
568 this AR event, it is important to assess the temporal evolution of the atmospheric circulation prior
569 to and during the event itself. This is achieved in Fig. 7, which shows multiple fields from 13 July
570 at 06 UTC to 15 July at 18 UTC. At 06 UTC on 13 July (Fig. 7a), a broad low-pressure system is
571 centered northwest of the site, coincident with a TPV (highlighted in the figure), with a ridge to its
572 east. The TPV helps the surface low to intensify, together with the jet streak at upper levels (Fig.
573 5c), with the central pressure dropping to around 944 hPa on 12 July at 12 UTC. The pressure
574 dipole promotes the southward advection of a warmer and moist low-latitude air mass into the
575 Southern Ocean, as noted by the hatching that highlights regions where the IVT exceeds $250 \text{ kg m}^{-1} \text{ s}^{-1}$.
576 A secondary low, which develops later on 13 July (highlighted in Fig. 7c, also noted by the
577 additional sea-level pressure contour), is not co-located with a TPV. Instead, the secondary low is
578 driven by the interaction of the warm and moist air mass from the west and northwest around the
579 low pressure with that from the northeast around the ridge. Closer to the Antarctic coast, the
580 aforementioned low-level convergence is reinforced by the drier and colder katabatic flow blowing
581 from the continent. The maximum Eady growth rate, a measure of baroclinicity (Hoskins and
582 Valdes, 1990), at 850 hPa exceeded 3 day^{-1} on 14 July (not shown), indicating a highly baroclinic
583 environment.

584

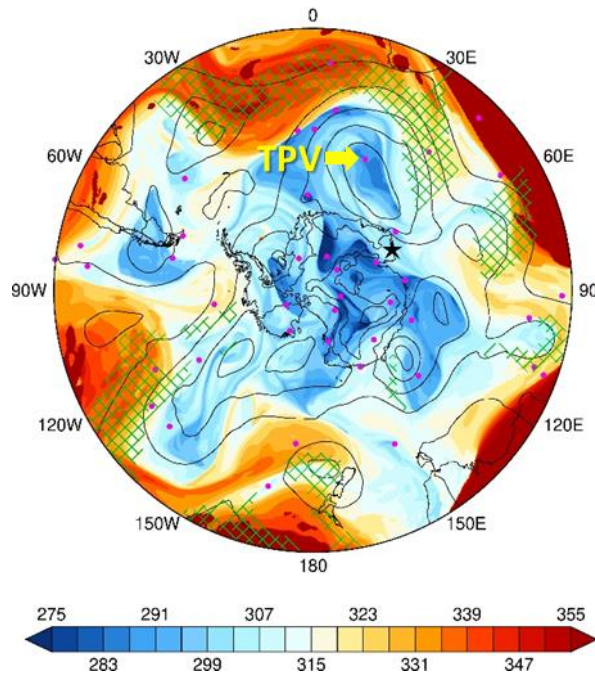
585 Figures 7b-d show cyclonic Rossby wave breaking, with the secondary low exhibiting little
586 eastward movement owing to the presence of a ridge to the east (Figs. 6a-b), and instead shifting
587 southwards towards Antarctica. The incursion of the higher low-latitude potential temperature
588 values into East Antarctica (Figs. 7b-d) is consistent with the warmer (Fig. 6d) and more moist
589 (Figs. 6a-c) conditions in the region. The warm and moist air intrusion shifted eastwards from 14
590 to 15 July (Figs. 7c-d) and penetrated deeper into East Antarctica on 15-16 July (Figs. 7d and 6d),
591 with air temperatures more than 15 K above climatology in some parts (Fig. 6d). Fig. 7 shows more
592 than one episode of intrusion of low-latitude air masses into Antarctica. For example, on 14-16
593 July a warm and moist air intrusion reached the Antarctic Peninsula (Figs. 7c-d). Such occurrences
594 are more common in an amplified pattern and can be aided by TPVs that act to strengthen the
595 attendant cyclone (Wille et al., 2024c).

596

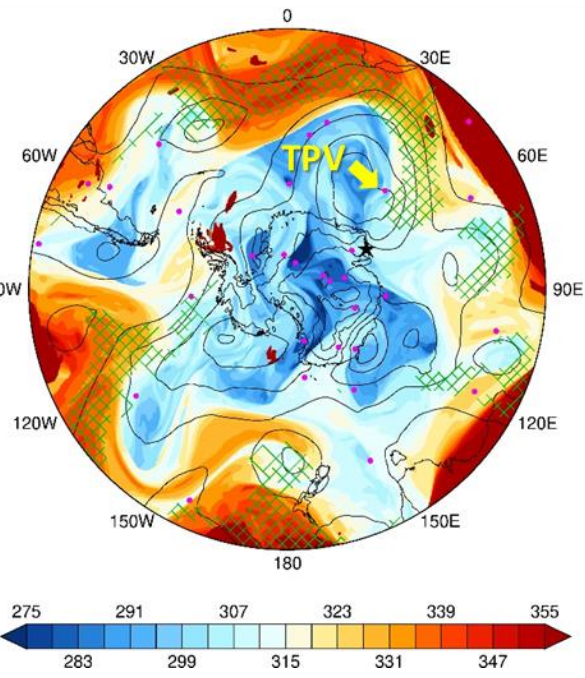
(a)

(b)

13 JULY 2022 @ 06 UTC

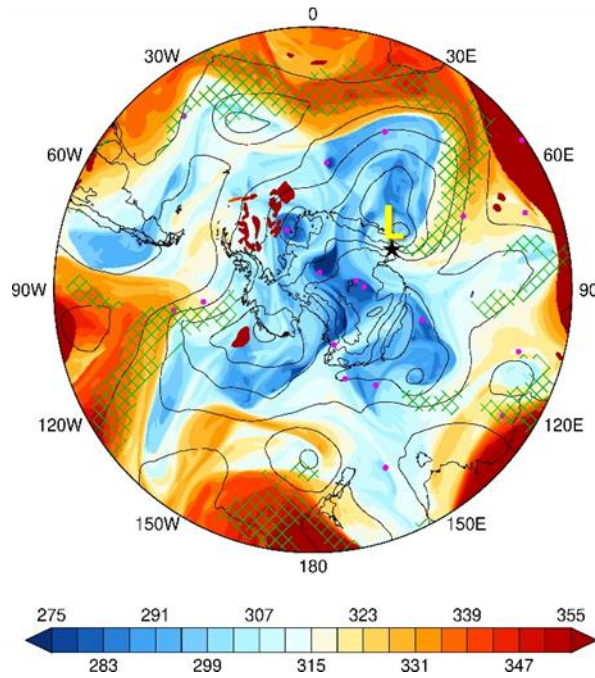


13 JULY 2022 @ 18 UTC



(c)

14 JULY 2022 @ 06 UTC



(d)

15 JULY 2022 @ 18 UTC

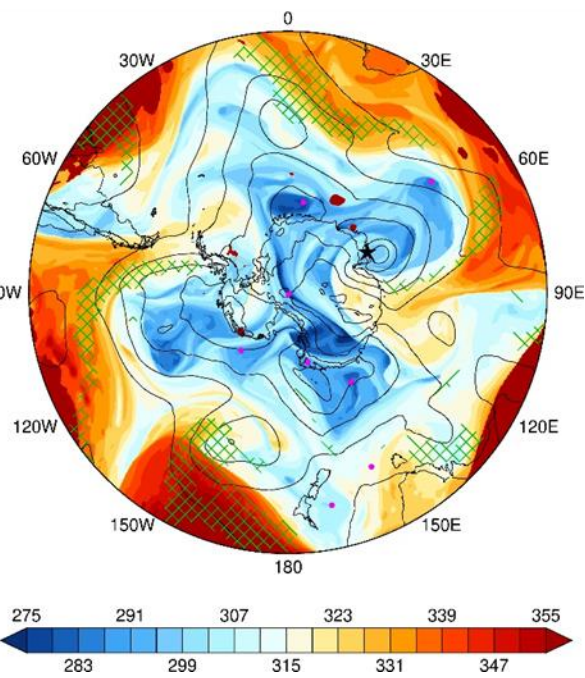


Figure 7: Evolution of Atmospheric State during 13-15 July 2022: Potential temperature (θ ; shading; K) on the dynamical tropopause (PV = -2 PVU), sea-level pressure (black contours; every 15 hPa starting at 900 hPa) and integrated vapour transport (IVT; hatching if $> 250 \text{ kg m}^{-1} \text{ s}^{-1}$) on 13 July at (a) 06 UTC

and (b) 18 UTC, (c) 14 July at 06 UTC, and (d) 15 July at 18 UTC. The purple dots indicate the location of tropopause polar vortices (TPV) at the respective times. The TPV and the secondary low pressure discussed in the text are highlighted in panels (a)-(b) and (c), respectively.

597

598 **4.2 PolarWRF Simulation**

599 In this subsection, the focus is on the modeling experiments. In Section 4.2.1, the PWRF
600 predictions are evaluated against *in-situ* measurements at the five stations in East Antarctica given
601 in Fig. 4b1d, while in Section 4.2.2 the emphasis is on the additional insight the higher-resolution
602 model data gives on the mid-July 2022 AR event.

603 **4.2.1 Evaluation of PolarWRF**

604 The PWRF simulations for 11-16 July 2022 are evaluated against *in-situ* meteorological
605 observations at the Mawson, Syowa, Relay, Davis and Casey stations, in addition to surface
606 radiation fields at Syowa Station. Fig. 8 shows the time-series of hourly data for the Mawson and
607 Syowa stations, with the corresponding time series for the other two stations given in Fig. S4. A
608 quantitative assessment of the model performance for all stations and variables is presented in
609 Table 3.

610

611 PWRF simulates the weather conditions well at the Mawson (Figs. 8a-f), Syowa (Figs. 8g-1
612 and S4a-f), Relay (Fig. S4g-l), Davis (Fig. S4m-r) and Casey (Fig. S4s-x) stations for 11-16 July
613 2022. In particular, the observed variability in sea-level pressure is well replicated, with the model
614 correctly capturing the time of passage and strength of the secondary cyclone on 14-15 July at
615 Mawson (Figs. 7c-d; Fig. 8c) and on 15 July at the Davis (Fig. 7d; Fig. S4p) Stations. Moreover,
616 the warmer, more moist and windier conditions on 12-14 July at Syowa Station (Figs. S4a-c and
617 S4f), on 14-15 July at Mawson (Fig. 8a-c and 8e) and Relay (Fig. S4g-i and S4l) Stations, and on
618 15-16 July at Davis (Fig. S4m-o and S4r) and Casey (Fig. S4s-u and S4x) Stations are predicted
619 by the model. Also, the model captures the increase in the downward long-wave radiation flux by
620 up to 80 W m^{-2} at Syowa Station (Fig. 8k) in association with the warm and moist air intrusion on
621 13-14 July. An inspection of Table 3 reveals that, and except mainly for the air temperature and
622 surface pressure, the normalized bias μ is smaller than 0.5, indicating the biases can be regarded
623 as not significant, while the normalized error variance α does not exceed 1 for all fields and stations
624 (except for the wind vector at the higher-elevation Relay and coastal Davis Stations), indicating
625 that the PWRF predictions can be regarded as trustful. The performance of PWRF for this event is
626 comparable to that for the McMurdo Station in early January 2016 (Hines et al., 2019), for West
627 Antarctica in early to mid-January 2019 (Bromwich et al., 2022), and for the Antarctic Peninsula
628 for May-June 2019 and January 2020 (Matejka et al., 2021). This reflects the improvements made
629 to PWRF by the model developers, with the aim of optimizing its performance and skill over
630 Antarctica (e.g., Hines et al., 2021).

631

632 A closer inspection of Figs. 8 and S4 and Table 3 reveals some discrepancies in the PWRF
633 predictions. For example, at Syowa Station, the model has a tendency to over-predict the air
634 temperature by \sim 1-3 K. This may explain the overestimation of the upward longwave radiation
635 flux by about 14.3 W m^{-2} (Fig. 8l), which can also arise from an overprediction of the observed
636 surface emissivity. The downward longwave radiation flu (Fig. 8k), on the other hand, is
637 underestimated by roughly 7.7 W m^{-2} , likely related to the reduced atmospheric moisture content
638 in the model by about $\sim 0.16 \text{ g kg}^{-1}$. At all four coastal Antarctica stations, the predicted wind
639 direction is generally shifted clockwise by 45° - 90° compared to that observed (Figs. 8d, S4e, S4q
640 and S4w), with this mismatch at times reaching 180° at the Relay Station (Fig. S4k) located on the
641 Antarctic plateau more than 3,000 m above sea-level (Fig. 1^bd). This discrepancy can be attributed
642 to an incorrect representation of the surface topography which exhibits a complex spatial
643 heterogeneity in the region (Lea et al., 2024). Despite these issues, both the magnitude and
644 variability of the observed wind speed are generally well represented by PWRF (Figs. 8e, S4f, S4l,
645 S4r, and S4x). The more offshore wind direction at the coastal Antarctica stations reflect a stronger
646 katabatic wind regime that acts to slow the poleward movement of the low-latitude air mass, which
647 is consistent with the dry bias of up to 0.2 g kg^{-1} . The positive mixing ratio bias at the Relay Station
648 occurs primarily on 15-16 July (Fig. S4h), and is associated with increased but still rather low
649 (generally below 0.1 g kg^{-1}) moisture levels advected from the interior of Antarctica. At all stations
650 except Mawson, PWRF exhibits a warm bias (Figs. 8a, 8g, S4g, S4m, and S4s), with the near-
651 surface wind speed being underestimated at Mawson (Fig. 8e) and overestimated at the other
652 stations (Figs. S4f, S4l, S4r, and S4x). Together with the dry bias, this suggests a tendency for
653 excessive boundary layer mixing in the model compared to observations, which has been reported
654 in a number of PWRF studies (e.g., Wille et al. 2016, 2017; Vignon et al., 2019). An optimized
655 PBL scheme, which at least partially corrects for the excessive mixing, and/or a more sophisticated
656 land surface model that more accurately represents the boundary layer and surface processes, have
657 to be considered to address the aforementioned biases. Despite this, PWRF captures the effects of
658 the AR as seen in observations, most notably the increase in air temperature and water vapour
659 mixing ratio, and the strengthening of the near-surface wind in particular at the more impacted
660 Mawson (Figs. 8a-e) and Davis (Figs. S4m-r) stations.

661
662 The SMB analysis performed using ERA-5 data is repeated using the hourly PWRF predictions.
663 Figs. S5a-b give the observed SIT and ST measurements, while Figs. S5c-d show the different
664 terms of the SMB as predicted by PWRF. PWRF The model gives a similar estimate of the
665 different terms of the components of the SMB with respect to the reanalysis dataset (cf. Figs. S5c-
666 da-b with 3i-jg-h), with the roughly 30% higher surface sublimation on 15 July arising from the
667 drier (\sim 10% lower relative humidity; cf. Figs. S5e-S5e with 3i3k) and windier (\sim 10% higher wind
668 speed; cf. Figs. S5d-S5f with 3j3l) near-surface conditions in the model. The fact that ERA-5
669 captures Foehn effects at this site and for this event, suggests that it can be used for the wider
670 analysis of Foehn events around East Antarctica, as has been done over West Antarctica (Francis
671 et al., 2023) and the Antarctica Peninsula (Laffin et al., 2021). The up to \sim 2 mm w.e. hr^{-1}
672 precipitation rate (Figs. S5a-S5c and 3g3i), \sim 5 K air temperature increase (Fig. S5e-S5e and 3i3k),

673 and 30 m s^{-1} wind speeds (Figs. S5d-S5f and 3j3l) associated with the passage of the AR on 14
674 July are simulated by PWRF, with the cold bias in the model also seen in comparison with *in-situ*
675 measurements at Mawson Station (Table 3).

676
677 Fig. 8f shows a comparison of the observed and simulated snow depth at the Khalifa SIMBA site
678 on fast ice off Mawson Station. The ST in PWRF is initialized to zero, and hence the discrepancy
679 with respect to the observed values during 11-13 July (the observed ST is equal to 0.14 m during
680 10-14 July). PWRF predicts around 0.24 m of snowfall in association with the passage of the AR
681 on 14 July, and the weaker wind speeds in the model, at times by more than 20 m s^{-1} , likely allow
682 for snow to accumulate at the site instead of it being blown away by the wind. The model fails to
683 capture the observed decrease of 0.02 m in ST on 15 July in response to Foehn effects, which can
684 be attributed to less favourable conditions for Foehn events in the model (e.g., ~~both with respect~~
685 ~~to the wind direction (west-southwesterly in PWRF as opposed to southeasterly in observations)~~
686 ~~the wind and speed is~~ lower by as much as 20 m s^{-1} , Fig. 8e, with generally cooler air temperatures,
687 Fig. 8a). A higher spatial resolution of at least 1 km would probably be needed for a more accurate
688 simulation of the interaction of the AR with the complex Antarctic topography including the Foehn
689 effects (Gilbert et al., 2025). The increase in ST on 16 July due to snowfall is simulated by PWRF,
690 even though its magnitude is underestimated by the model (0.01 m in PWRF as opposed to 0.04 m
691 in observations), possibly because of the drier environment brought on by a more offshore wind
692 direction (Figs. 8b, 8d-e, and S5e-f~~b-d~~). ~~It is important to stress that the discrepancies between the~~
693 ~~observed and modelled ST can also be tied to deficiencies in the LSM. In particular, the Noah~~
694 ~~LSM used in this study only considers a single snow layer and has a simplified representation of~~
695 ~~snow accumulation, sublimation, and melting processes (Lim et al., 2022). In contrast, the more~~
696 ~~sophisticated Noah LSM with multiparameterization options (Noah-MP), also available in PWRF~~
697 ~~and that features user-defined parameters, includes up to three snow layers, represents the~~
698 ~~percolation, retention, and refreezing of meltwater within the snowpack, and accounts for snow~~
699 ~~metamorphism and compaction (Niu et al., 2011). Recent work has shown that it gives a superior~~
700 ~~performance with respect to the Noah LSM over Antarctica with respect to the 2-m temperature~~
701 ~~and 10-m wind speed forecasts (Xue et al., 2022). An extension of this work would be to consider~~
702 ~~the Noah-MP and explore its effects on the ST predictions.~~

703
704 Besides ground-based observations, sounding data are available at the Mawson, Syowa, Davis,
705 and Casey stations every 12 h and can be compared with the hourly PWRF predictions (Figs. S6
706 and S7). The model captures the timing of the arrival of the warm and moist air mass at Mawson
707 on 14-15 July, as evidenced by the higher values of θ_E (270-280 K; Figs. S6a and S6e) and relative
708 humidity (60-90%; Figs. S6b and S6f). However, the katabatic wind flow is stronger in the model
709 as seen by the offshore wind direction (Fig. S6h) and drier conditions (Figs. S6b and S6f), and also
710 evident in the ground-based observations (Figs. 8d and 8b), with a strong low-level jet (mostly
711 below 700 hPa) on 14 and 16 July (Fig. S6g). At Syowa, the PWRF and observed profiles are in
712 closer agreement than at the Mawson Station (cf. Figs. S6a-h with S6i-p). Here, the main

discrepancy between the observed and modelled profiles is the dry bias (Figs. S6j and S6n), which is more pronounced on 13-14 July, and is also evident in the near-surface data (Fig. 8i). The arrival of the low-latitude air mass at Davis on 15 July is seen in both the PWRF and observed profiles (Figs. S7a-h), with a less pronounced katabatic regime in the model compared to that at Mawson Station (cf. Figs. S6e-h with S7e-h). At Casey (Figs. S7i-p), PWRF simulates the more moist conditions on 14 July and the drier conditions on 15-16 July. The analysis of the sounding profiles reveals, however, that PWRF tends to overestimate the strength of the katabatic flow over coastal East Antarctica during 11-16 July. Vignon et al. (2019) attribute such overestimates to more stable boundary layers over the Antarctic Plateau and, to a lesser extent, steeper synoptic land-ocean pressure gradients in the model.

723
724
725
726
727

The results in Figs. 8, S4-S7, and Table 3 reveal a reasonably good PWRF performance in the study area for the period 11-16 July 2022. In the next subsection, the model simulations are used to gain further insight into the dynamics of the 14 July AR event.

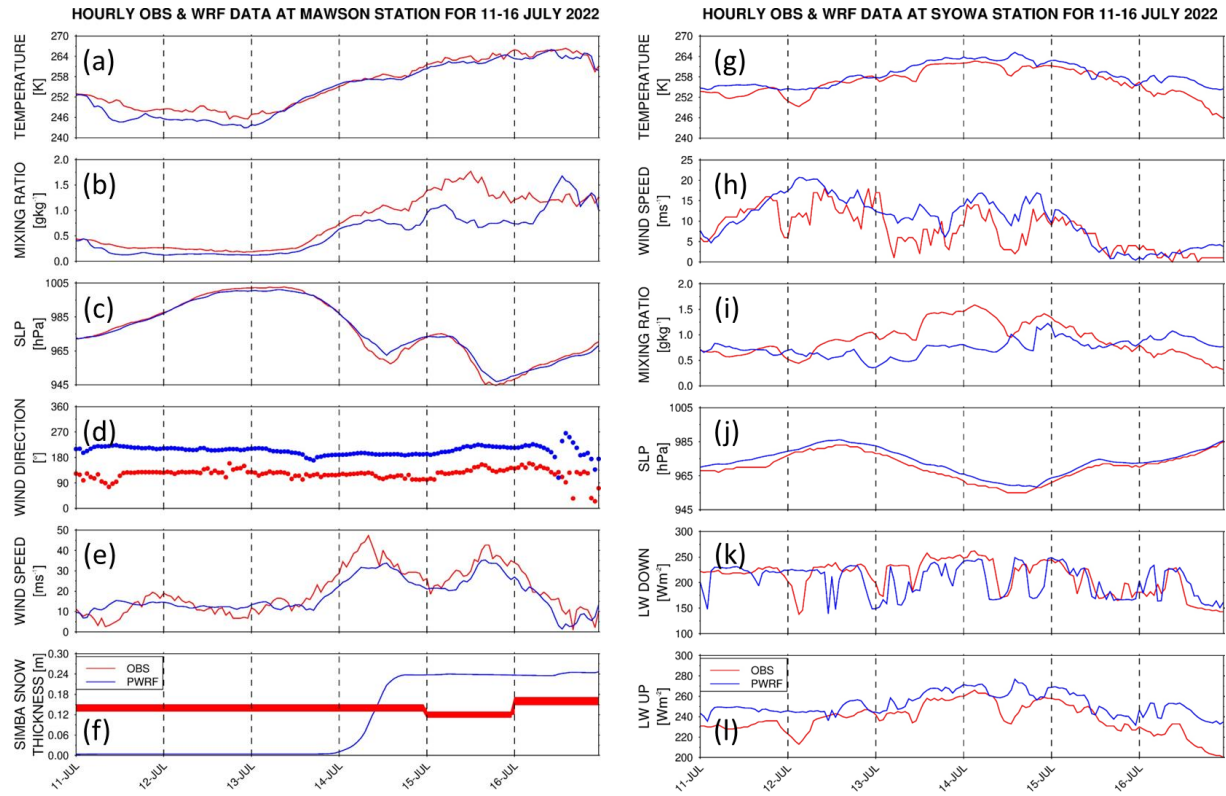


Figure 8: Evaluation of PolarWRF against ground-based observations: Hourly (a) air temperature ($^{\circ}\text{C}$), (b) water vapour mixing ratio (g kg^{-1}), (c) sea-level pressure (SLP; hPa), and horizontal wind (d) direction ($^{\circ}$) and (e) speed (m s^{-1}) from observations (red) and the PWRF simulation (blue) for 11-16 July 2022 at Mawson Station. (f) shows the daily observed (red) and hourly PWRF-predicted (blue) ST (m) at the Khalifa SIMBA site on fast ice off Mawson Station, the former with the estimated 7% uncertainty. (g)-(l) is as (a)-(f) but for the hourly air temperature (K), horizontal wind speed (m s^{-1}), water vapour mixing ratio (g kg^{-1}), sea-level pressure (SLP; hPa), and surface downward and upward longwave

radiation fluxes (W m^{-2}), respectively at Syowa Station. The wind fields at Syowa Station are shown in Figs. S4e-f. The location of the stations is given in Fig. [1b1d](#).

728
729

Variable	Station	Bias	μ	ρ	η	α
Air Temperature	Mawson	-1.42 K	-0.92	0.98	~1.0	0.02
	Syowa	2.15 K	1.08	0.87	0.98	0.14
	Relay	2.51 K	0.65	0.90	~1.0	0.10
	Davis	3.11 K	1.30	0.98	0.97	0.05
	Casey	2.66 K	1.22	0.75	0.97	0.27
Water Vapour Mixing Ratio	Mawson	-0.21 g kg^{-1}	-0.82	0.86	0.98	0.16
	Syowa	-0.16 g kg^{-1}	-0.45	0.05	0.82	0.96
	Relay	0.01 g kg^{-1}	0.69	0.75	0.99	0.25
	Davis	-0.09 g kg^{-1}	-0.28	0.97	0.94	0.08
	Casey	-0.02 g kg^{-1}	-0.12	0.61	0.92	0.43
Wind Vector (Bias and μ are for wind speed)	Mawson	-2.39 m s^{-1}	-0.48	0.27	0.96	0.74
	Syowa	2.36 m s^{-1}	0.61	0.39	~1.0	0.61
	Relay	2.02 m s^{-1}	1.82	-0.60	~1.0	1.60
	Davis	1.40 m s^{-1}	0.36	-0.30	0.99	1.29
	Casey	0.79 m s^{-1}	0.24	0.08	0.98	0.93
Surface Pressure	Mawson	-3.78 hPa	-1.72	0.99	~1.0	0.01
	Syowa	3.08 hPa	2.35	0.99	~1.0	0.01

	Relay	2.53 hPa	3.16	0.99	0.99	0.02
	Davis	-0.74 hPa	-0.50	~1.0	~1.0	0.01
	Casey	-2.48 hPa	-2.16	~1.0	0.99	0.01
Downward LW	Syowa	-7.71 W m^{-2}	-0.24	0.47	~1.0	0.53
Upward LW	Syowa	14.26 W m^{-2}	1.54	0.79	0.95	0.25

730
731
732
733
734
735
736
737
738

Table 3: Verification diagnostics with respect to station data: Bias, normalized bias (μ), correlation (ρ), variance similarity (η), and normalized error variance (α) for air temperature, water vapour mixing ratio, horizontal wind vector and sea-level pressure for Mawson, Syowa, Relay, Davis, and Casey Stations for 11-16 July 2022. For Syowa Station, the scores are also given for the surface downward and upward longwave radiation fluxes at the bottom of the table. The model values are those at the closest grid-point to the location of the station, and the evaluation is performed for hourly data. The correspondent time-series are given in Figs. 8 and S4.

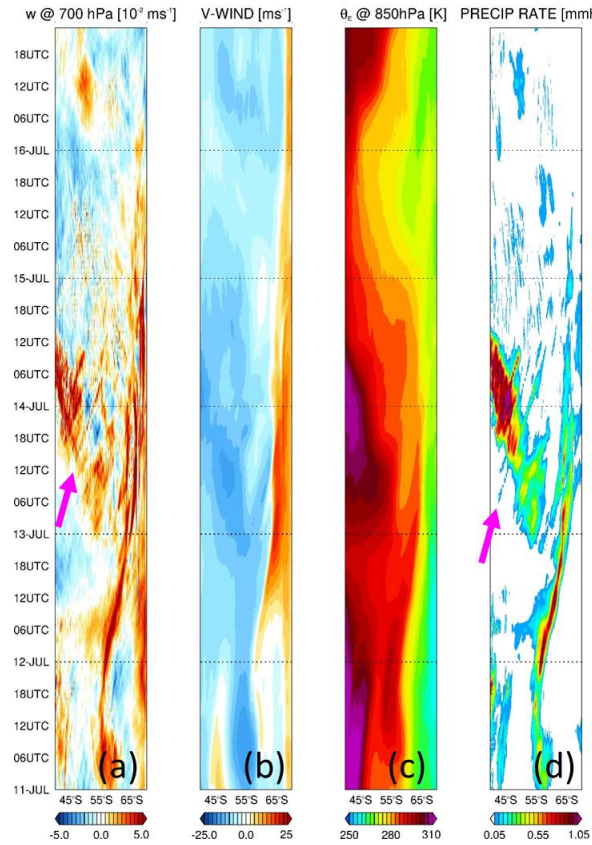
739 4.2.2 Insights into the Dynamics and Effects of the AR

740 One of the motivations for implementing the high-resolution (2.5 km) innermost grid is to
741 check for the presence of AR rapids (Box et al., 2023; Francis et al., 2024). Figs. 9a-d show a
742 hovmoeller plot of the vertical velocity at 700 hPa, 10-m meridional wind speed, 850 hPa
743 equivalent potential temperature (θ_E), and precipitation rate averaged over 40°-50°E, a latitude
744 band that comprises the bulk of the AR (Figs. 6a, 7a-c and 9i). It reveals AR rapids, in particular
745 one on 13-14 July between 40°-60°S (pink arrows in Figs. 9a and 9d), which is embedded within
746 the AR, as seen on 13 July at 12 UTC when it is located at 40°-50°S (Fig. 9i). No AR rapids are
747 seen in the vertical profiles at the coastal Antarctic stations (Figs. S6 and S7), suggesting they are
748 confined to the Southern Ocean. The linear structure propagating from ~55°S late on 11 July to
749 65°S early on 13 July does not correspond to an AR rapid. Instead, the heavy precipitation ($>1 \text{ mm}$
750 hr^{-1} ; Fig. 9d) arises from the interaction of the low-latitude air mass with the katabatic wind regime
751 originating from the Antarctic Plateau, as it is placed at the interface between the two flows (cf.
752 Figs. 9a-b with 9d). The low-level convergence of these two air masses can be seen in Fig. 9i
753 around 65°S. The katabatic flow is characterized by southerly winds (Fig. 9b) and low θ_E values
754 (260-270 K, compared to 290-300 K for the low-latitude air mass; Fig. 9c), extending from the
755 Antarctic Plateau to the Southern Ocean. Figs. 9e-h are as Figs. 9a-d but the fields are averaged
756 over 85°-95°E. The low-latitude air mass reaches this part of East Antarctica on 15-16 July, when
757 precipitation rates exceed $1.8 \text{ mm w.e. hr}^{-1}$. The maximum precipitation rate in coastal Antarctica
758 and averaged over 85°-95°E is about 66% higher than that averaged over 40°-50°E (1.81 vs. 1.09
759 mm w.e. hr^{-1}). This can be explained by (1) the higher moisture levels (maximum longitudinally-

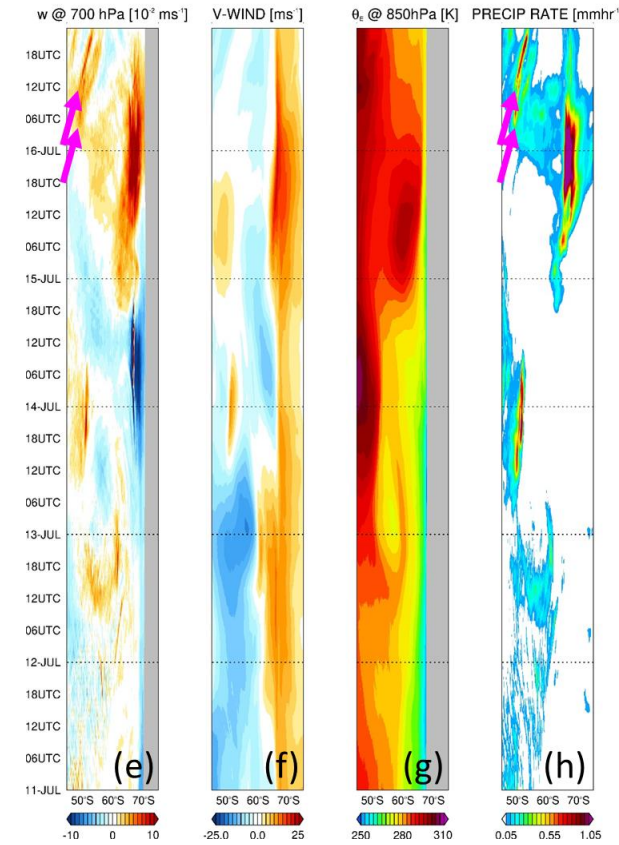
760 averaged θ_E values of 297.9 K vs. 289.7 K), as the low-latitude air mass penetrates further
761 polewards due to a more favourable synoptic pressure pattern, and (2) a stronger katabatic flow
762 off the Antarctic Plateau (maximum longitudinally-averaged meridional wind speed of 22 m s^{-1} vs.
763 19 m s^{-1}). Around 45° - 55°S on 16 July, AR rapids are present in the plots averaged over 85° - 95°E
764 (pink arrows in Figs. 9e and 9h), when the low-level air intrusion was in the area (Fig. 9j). The
765 fact that these structures have been identified in modelling products in the Southern Ocean in this
766 study, around Greenland in Box et al. (2023), and in the Middle East in Francis et al. (2024),
767 stresses the need for high spatial and temporal resolution three-dimensional radar observations
768 along the ARs to check whether they actually exist or are just model artefacts.

769

HOVMOELLER PLOTS AVERAGED OVER 40°-50°E FOR 11-16 JULY 2022



HOVMOELLER PLOTS AVERAGED OVER 85°-95°E FOR 11-16 JULY 2022



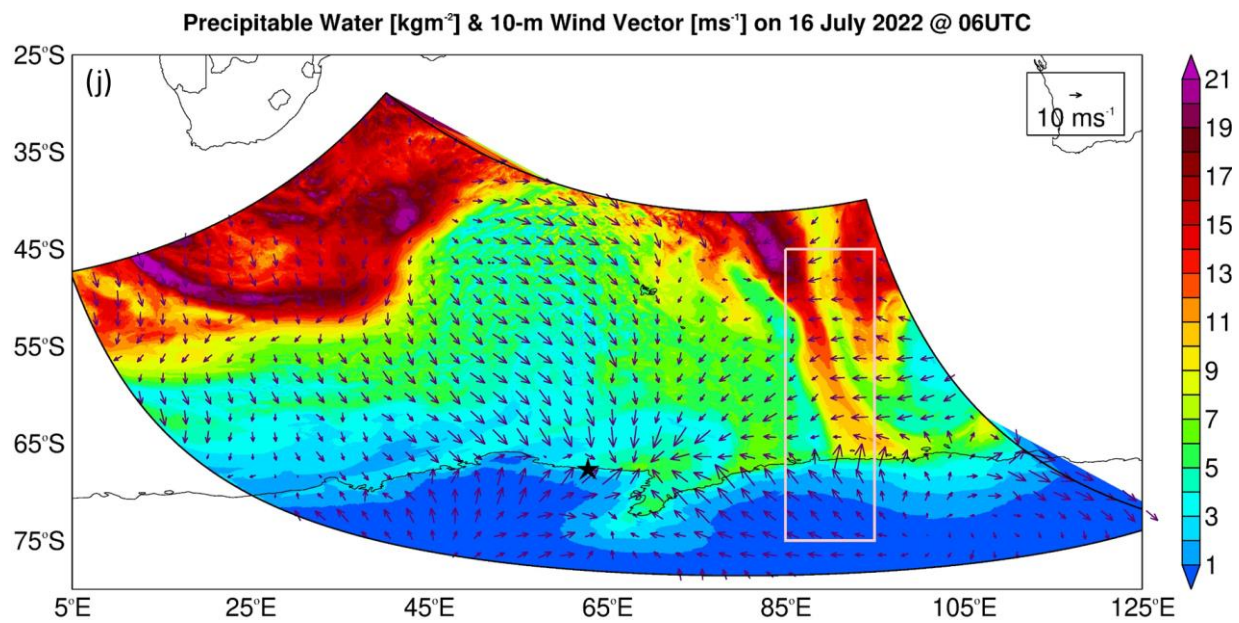
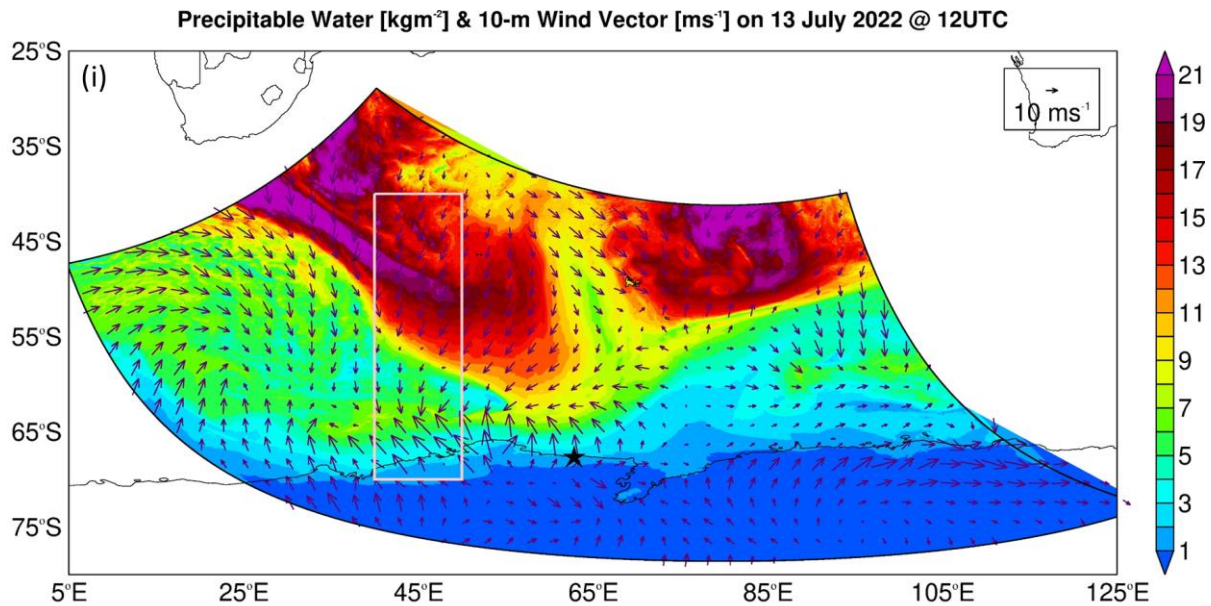


Figure 9: Hovmoeller Plots: Hovmoeller of hourly (a) 700 hPa vertical velocity (10^{-2} m s^{-1}), (b) 10-m meridional wind speed (m s^{-1}), (c) 850hPa equivalent potential temperature (θ_E ; K), and (d) precipitation rate (mm hr^{-1}) for 11-16 July 2022 averaged over 40° - 50° E. The pink arrows highlight AR rapids. (e)-(h) are as (a)-(d) but averaged over 85° - 95° E. The grey shading in (e) and (g) highlights latitudes for which the 700 hPa and 850 hPa pressure levels, respectively, are below topography. (i) Precipitable water (shading; kg m^{-2}) and 10-m wind vector (arrows; m s^{-1}) at 12 UTC on 13 July. The star indicates the

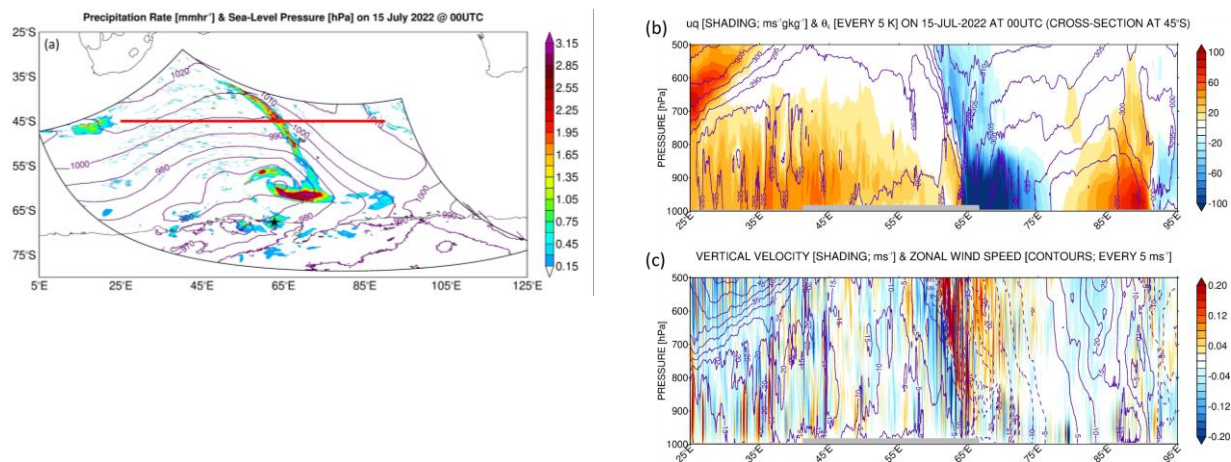
location of Mawson Station. The fields given in (a)-(d) are averaged over the longitude band of the pink box (40° - 50° E) and plotted over its latitude range. (j) is as (i) but at 06 UTC on 16 July, with the pink box also giving the latitude range over which the fields in (e)-(h) are plotted, and its longitude band (85° - 95° E) that used for averaging to generate the hovmoeller plots.

770

771 On top of surface evaporation from the subtropics (Fig. S2), the convergence of the flow
 772 around the low-pressure system to the west and the ridge to the east helped feed the AR and
 773 associated warm and moist air mass (Fig. 7). This can be seen in Figs. 10a-c. The zonal moisture
 774 transport in Fig. 10b highlights the convergence of the westerly flow at 5 - 10 $m\ s^{-1}$ associated with
 775 θ values of 290 - 295 K, with the easterly flow around the high with zonal wind speeds of 20 - 25 m
 776 s^{-1} and θ_E values of 300 - 305 K, as this air mass comes directly from the tropics. At about 65° E,
 777 where the AR is located (Fig. 10a), the vertical velocity peaks in the mid-troposphere around 600 -
 778 800 hPa with speeds up to $0.3\ m\ s^{-1}$ (Fig. 10c). The vertical structure of the updrafts, with a peak in
 779 the low-to-mid troposphere, and the updraft speeds are comparable to the AR rapids reported by
 780 Box et al. (2023) over Greenland on 14 September 2017. Precipitation rates in excess of $3\ mm\ hr^{-1}$
 781 are simulated by the model at 12 UTC on 14 July (Fig. 10d) and at 00 UTC on 15 July (Fig. 10a)
 782 along the AR. As the moisture plume moved closer to the Antarctic coast, it interacted with the
 783 katabatic wind regime. This is evident in Figs. 10e-f, with the colder, drier ($\theta_E \sim 260$ - 265 K) and
 784 strong (meridional wind speeds in excess of $45\ m\ s^{-1}$) airflow from Antarctica, which descends the
 785 steep slopes with downward vertical velocities up to $-0.6\ m\ s^{-1}$, converging with the slower (35 - 40
 786 $m\ s^{-1}$) and more moist ($\theta_E \sim 275$ - 280 K) flow from lower-latitudes with vertical velocities in the
 787 bottom 5 km reaching $+0.3\ m\ s^{-1}$. This convergence led to precipitation rates in excess of $3\ mm\ hr^{-1}$
 788 around Mawson Station (Fig. 10d).

789 The results in Figs. 9 and 10 suggest that it can be difficult for ARs and associated warm and moist
 790 air intrusions to reach this region of East Antarctica owing to the interaction with the strong
 791 katabatic flow. This factor has been highlighted for other regions of East Antarctica (e.g., Terpstra
 792 et al., 2021; Gehring et al., 2022).

793



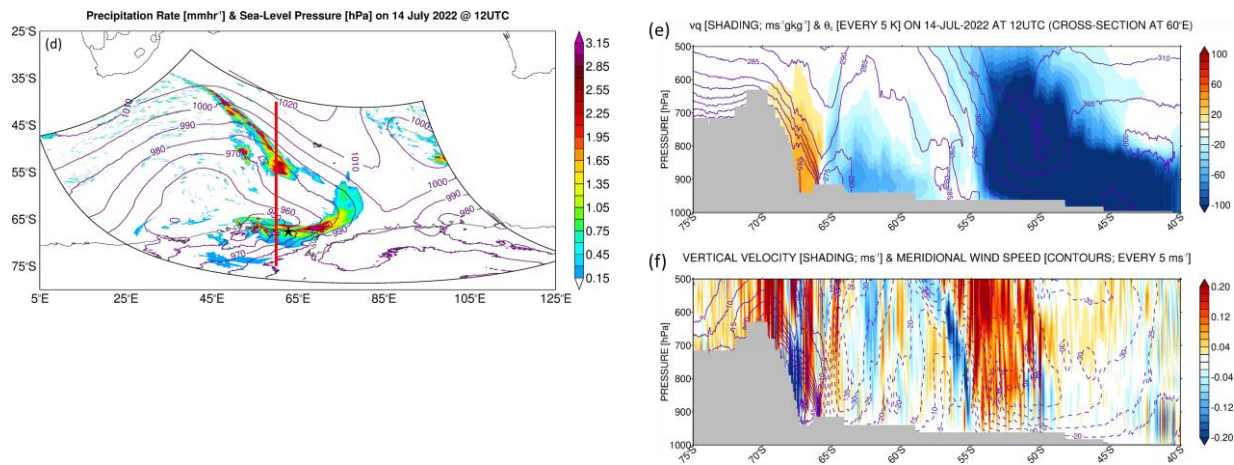


Figure 10: Precipitation mechanisms in the Southern Ocean: (a) Precipitation (shading; mm hr^{-1}) and sea-level pressure (contours; hPa) at 00 UTC on 15 July 2022, from PWRF's 2.5 km grid. Vertical cross-section at 45°S, red line in (a), of (b) zonal mass transport (shading; $\text{m s}^{-1} \text{g kg}^{-1}$) and equivalent potential temperature (θ_E ; contours; every 5 K), and (c) vertical velocity (shading; 10^{-2} m s^{-1}) and zonal wind speed (contours; every 5 m s^{-1}), at the same time. Regions below the orography are shaded in grey. (d)-(f) are as (a)-(c) but at 12 UTC on 14 July. The cross-section is at 60°E, with the meridional mass transport and meridional wind speed in (e) and (f) plotted instead of their zonal counterparts, respectively.

794

795 **5. Discussion and Conclusions**

796 Sea ice is a critically important component of the climate system, modulating atmosphere-
 797 ocean interactions and ultimately the global climate (Raphael et al., 2011; Goosse et al., 2023).
 798 Antarctic SIE has abruptly dropped from 2016 to 2019 (Eayrs et al., 2021; Yang et al., 2021) with
 799 an all time-record low in 2023, driven by a complex and as yet poorly-understood combination of
 800 oceanic and atmospheric processes (Wang et al., 2024b). Climate model projections indicate major
 801 changes in the atmospheric circulation driven by the projected reduction in Antarctic sea ice in a
 802 warming climate: the Polar Cell and the katabatic flow off the coast of Antarctica are projected to
 803 strengthen, with a marginal weakening of the Ferrel and Hadley cells, and an equatorward shift in
 804 the position of the Polar Jet (Tewari et al., 2023). This stresses the need for a much-improved
 805 understanding of the observed variability of sea-ice properties, such as the SIE and SIT that are
 806 highly heterogeneous around Antarctica, [in order](#) to increase confidence in future climate-change
 807 projections. [This is achieved in this study at a coastal site in East Antarctica through *in-situ*](#)
 808 [measurements for the period July-November 2022.](#)

809

810 The SIT at the Khalifa SIMBA site on fast ice off Mawson Station largely follows the annual
 811 seasonal cycle, with a gradual increase during winter to mid-to-late October followed by a steady
 812 decline in late spring. The maximum values of ~1.1-1.2 m are in the 0.50-1.50 m range estimated
 813 from satellite altimeter products for fast ice in the region around the Mawson Station (Li et al.,
 814 2022) and are also comparable to the thickness of pack ice around Antarctica (Kurtz and Markus,

815 2012; Kacimi and Kwok, 2020). The ST, on the other hand, is highly variable, with values in the
816 range 0.02-0.18 m; these are also consistent with the estimates from satellite altimetry. In contrast
817 to SIT, the temporal variability of ST is strongly linked to atmospheric forcing, in particular to
818 precipitation (snowfall), Foehn effects, blowing snow, and episodic warm and moist air intrusions,
819 which can lead to variations of up to ± 0.08 m in a day. During July-November 2022, an AR
820 impacted the site on 14 July. It led to an 18 K increase in air temperature within 24 h, and a
821 variation of up to 0.04 m in ST due to Foehn effects and snowfall (the 0.02 m change in SIT is
822 within the estimated uncertainty range). These changes occurred within one day of the AR's
823 arrival, followed by a recovery to pre-AR levels in the following 1-2 days. However, it is important
824 to stress that a longer observational period would be needed to establish more robust and
825 statistically significant links between atmospheric phenomena such as Foehn effects, blowing
826 snow, and incursions of warm and moist low-latitude air and the coastal ST (and potentially SIT).
827 In addition, having measurements for at least a full year would allow for the quantification of the
828 potential role of surface melting in ST and SIT, which is more likely in the summer months but
829 may occur at other times in a warming climate. Simulations with coupled ocean-atmosphere-sea-
830 ice models should also be considered to further explore the role of atmospheric forcing in ST and
831 SIT. In addition, refined methods to extract SIT and ST are desirable, as in particular for SIT, the
832 variation during weather events such as the passage of the AR is within the uncertainty range,
833 preventing a clear signal from being extracted from the data.

834
835 The 14 July AR is particularly intense, with the highest IVT around the Khalifa SIMBA site
836 on fast ice off Mawson Station of $\sim 156 \text{ kg m}^{-1} \text{ s}^{-1}$, which is in the top 0.5% of the climatological
837 distribution. This AR has its origins in South America, where a wavetrain coming from the Pacific
838 Ocean leads to an intensification of the South American Low-Low-Level Jet and increased
839 moisture outflow into the South Atlantic Ocean. The period 10-19 July 2022 is characterized by a
840 wavenumber #5 pattern along the subtropical jet and a wavenumber #3 along the polar jet in the
841 Southern Hemisphere, the latter projecting into the positive SAM phase, which is expected given
842 the ongoing La Niña. A pressure dipole, with a low to the west and a ridge to the east, promotes
843 the advection of warm and moist low-latitude air across Mawson Station. A back-trajectory
844 analysis indicates contributions from evaporation both in the subtropics and the Southern Ocean
845 to the precipitation event on 14 July 2022. A more in-depth analysis reveals that a secondary low
846 formed just northwest of the site on 13 July, driven by high baroclinicity arising from the
847 interaction of the warmer low-latitude air masses with the cold katabatic winds that prevail around
848 Mawson Station. At the same time, a TPV and a jet streak at upper-levels contributed-contribute
849 to an intensification of the primary low. The changing wind field in response to the passage of the
850 deep cyclone, which had a central pressure as low as 931 hPa, also has an impact on the sea-ice
851 dynamics. In particular, maximum pack-ice drift velocities north of Mawson Station exceeded 40
852 km day^{-1} from 12-14 July and 20 km day^{-1} from 14-16 July with the opening of a polynya in the
853 Southern Ocean northwest of Mawson Station around $65^\circ\text{S}, 45^\circ\text{E}$ from 14 to 22 July. These pack-

854 ice drift speeds are comparable to those estimated during the opening of the Maud Rise Polynya
855 in September 2017 (Francis et al., 2019).

856

857 A high-resolution simulation with PWRF down to 2.5 km is conducted to gain further insight
858 into this event. An evaluation against *in-situ* observations indicates a good performance for both
859 coastal and inland stations in the target region. A dry bias at coastal sites is attributed to an
860 excessive offshore wind direction in the model and/or too much boundary layer mixing. An
861 evaluation of the simulated vertical profiles against those observed at four coastal sites reveals a
862 stronger katabatic flow in PWRF, which is consistent with the drier near-surface conditions.
863 This is reported by other studies (e.g., Vignon et al., 2019), which attributed it to more stable
864 boundary layers over the Antarctic Plateau and steeper land-sea synoptic pressure gradients. The
865 overestimation of the surface upward longwave radiation flux may be a reflection of higher surface
866 temperatures and/or a too high surface emissivity in PWRF. This suggests the need to optimize the
867 land surface properties in the model, as has been highlighted by other studies (Hines et al., 2019).
868 Ingesting a more realistic representation of the SIE and SIT does not translate into higher skill
869 scores for this particular event. This indicates that improvements to the boundary layer dynamics
870 and/or land/ice processes, noted by Wille et al. (2016, 2017) and Vignon et al. (2019), and at least
871 for this case study, are probably more important than having a more accurate sea-ice representation
872 in the model. Besides calibrating surface parameters, future PWRF studies should explore other
873 physics schemes and/or optimize the tunable parameters defined inside the selected ones, in
874 particular in the PBL and [land-surface modelLSM](#) as done for other regions (e.g., Quan et al.,
875 2016; Chinta and Balaji, 2020), in an attempt to improve the model performance. [For example, the](#)
876 [LSM employed, Noah LSM, has a simplified representation of snow processes compared to the](#)
877 [more sophisticated Noah-MP \(Niu et al., 2011\), which has shown higher skill over Antarctica \(Xue](#)
878 [et al., 2022\). Adding a higher-resolution nest over the target region can also be beneficial as it will](#)
879 [allow for a more accurate representation of dynamic and thermodynamic processes \(Gilbert et al.,](#)
880 [2025\).](#) The high-resolution PWRF simulation [revealed-reveals](#) the presence of AR rapids, with a
881 similar vertical structure and propagation speed as those reported in Box et al. (2023) over
882 Greenland in September 2017. The model simulation also [highlighteds](#) the effects of the katabatic
883 wind regime in slowing down and weakening the low-latitude warm and moist air incursions as
884 they approach the Antarctic coast. It is this interaction that triggers precipitation rates in excess of
885 3 mm hr⁻¹ around Mawson Station during 14 July AR.

886

887 The SIMBA deployment at a fast ice site off Mawson Station during July-November 2022
888 enabled a better understanding of the spatial and temporal variability of SIT and ST in that part of
889 coastal East Antarctica. Such measurements should also be conducted at other sites given the
890 marked regional differences in sea-ice properties in the Southern Ocean (Parkinson and Cavalieri,
891 2012). This will also help to evaluate and improve the ST, SIE and SIT estimates derived from
892 satellite remote sensing and numerical models. Besides ocean dynamics and thermodynamics, the
893 findings of the study stress the role of atmospheric forcing in driving the variability [in particular](#)

894 of ST ~~in particular~~. Long-term measurements are needed to further explore and quantify how
895 Foehn effects, blowing snow, warm and moist air intrusions, and surface melting modulate SIT
896 and ST, and how they respond to seasonal and inter-annual variations in the atmospheric and
897 oceanic state. This is a crucial step to improving the quality and confidence of future climate-
898 change projections and medium- and long-range weather forecasts owing to the global influence
899 of sea-ice variability on the climate system.

900

901 **Acknowledgements**

902 This work was funded by Khalifa University Polar Research Center. The authors wish to
903 acknowledge the contribution of Khalifa University's high-performance computing and research
904 computing facilities to the results of this research. The SIMBA deployment at a fast ice site the
905 Mawson Station, *in-situ* measurements and the technical assistance were supported under
906 Australian Antarctic Science [AAS] Project #4506 (CI: P. Heil). The work of P. Heil and R.
907 Massom was supported by the Australian Antarctic Division. For R. Massom, this work was also
908 supported by the Australian Research Council Special Research Initiative the Australian Centre
909 for Excellence in Antarctic Science (Project Number SR200100008). PH acknowledges support
910 from the AAS Program (AAS4496, AAS4506, AAS4625) and grant funding from the International
911 Space Science Institute (Switzerland; Project 405) and the Swiss Federal Research Fellowship
912 program. For P. Heil and R. Massom, this work contributes to Project 6 of the Australian Antarctic
913 Program Partnership (ASCI00002) funded under the Australian Government's Antarctic Science
914 Collaboration Initiative program. We are also grateful for the Byrd Polar and Climate Research
915 Center at The Ohio State University for developing and maintaining PolarWRF and making it
916 freely available to the scientific community. We greatly appreciate the support of the Automatic
917 Weather Station Program and the Antarctic Meteorological Research Center for the weather station
918 data used in this study (National Science Foundation grants numbers ARC-0713843, ANT-
919 0944018, and ANT-1141908). The authors also gratefully acknowledge the National Oceanic and
920 Atmospheric Administration Air Resources Laboratory for the provision of the Hybrid Single-
921 Particle Lagrangian Integrated Trajectory (HYSPLIT) transport and dispersion model used in this
922 work. We would like to thank the editor and two anonymous reviewers for their insightful and
923 constructive comments and suggestions that helped to substantially improve the quality of this
924 work.

925

926 **Code/Data availability**

927 The sea-ice and snow thickness measurements at the Khalifa SIMBA site on fast ice off Mawson
928 Station for July-November 2022 are available upon request from the corresponding author (Diana
929 Francis; diana.francis@ku.ac.ae). The remaining observational and the reanalysis datasets used in

930 this study are freely available online: (i) ERA-5 reanalysis data were downloaded from the
931 Copernicus Climate Data Store website (Hersbach et al., 2023a,b); (ii) Automatic Weather Station
932 (AWS) data at the Mawson, Davis, and Casey Stations can be requested at the Australian Antarctic
933 Data Center website (AADC, 2022); (iii) AWS and surface radiation data for Syowa Station were
934 obtained from the World Radiation Monitoring Center - Baseline Surface Radiation Network
935 website (AWI, 2024); (iv) AWS data for the Relay Station was extracted from the Antarctic
936 Meteorological Research Center & Automatic Weather Stations Project (Lazzara, 2024); (v) sea-
937 ice velocity vectors from the low resolution sea-ice drift product are available at the European
938 Organization for the Exploitation of Meteorological Satellites (EUMETSAT) Ocean and Sea Ice
939 Satellite Application Facility (EUMETSAT, 2024); (vi) sea-ice concentration maps derived from
940 the measurements collected by the Advanced Microwave Scanning Radiometer (AMSR) for Earth
941 Observing Systems instrument onboard the National Aeronautics and Space Administrations
942 (NASA) Aqua satellite and the AMSR-2 instrument onboard the Japan Aerospace and Exploration
943 Agency Global Change Observation Mission 1st-Water “Shizuku” satellite from January 2013 to
944 present, were obtained from the University of Bremen website (UoB; 2024); (vii) twice daily
945 atmospheric sounding profiles at the Mawson, Syowa, Davis, and Casey stations were accessed at
946 the University of Wyoming website (Oolman, 2025). The Hybrid Single-Particle Lagrangian
947 Integrated Trajectory (HYSPLIT) transport and dispersion model is downloaded from the National
948 Aeronautic and Space Administration Air Resources Laboratory website (NOAA ARL, 2024). The
949 PolarWRF model version 4.3.3 is available at the Byrd Polar and Climate Research Center at The
950 Ohio State University website (PWRF, 2024). The figures presented in this manuscript have been
951 generated with the Interactive Data Language (IDL; Bowman, 2005) and MATLAB (Mathworks,
952 2024) software.

953

954 Competing interests

955

956 One co-author is a member of The Cryosphere editorial board.

957

958 Author Contributions: CRediT

959 **DF**: Conceptualization of the study, Interpretation and validation of the results, Writing the draft,
960 Funding Acquisition; **RF**: Formal analysis, Data processing and analysis of the results, Writing
961 the draft; **NN**: Data acquisition, processing and analysis, Interpretation of the results, Inputs to the
962 manuscript; **PH**: Interpretation of the results, Inputs to the manuscript; **JDW**: Interpretation of the
963 results, Inputs to the manuscript; **IVG**: Interpretation of the results, Inputs to the manuscript;
964 **RAM**: Interpretation of the results, Inputs to the manuscript. All authors interpreted the results and
965 provided input to the final manuscript.

966

967

968 **References**

- 969 AADC (2022) Antarctic Climate Data Collected by Australian Agencies. Australian Antarctic Data Center
970 [Dataset]. Accessed on 22 April 2024, available online at [Australian Antarctic Data Centre \(aad.gov.au\)](https://www.aad.gov.au).
- 971
- 972 Alapaty, K., Herwehe, J. A., Otte, T. L., Nolte, C. G., Bullock, O. R., Mallard, M. S., Kain, J. S., Dudhia,
973 J. (2012) Introducing subgrid-scale cloud feedbacks to radiation for regional meteorological and climate
974 modeling. *Geophysical Research Letters*, 39, L24809. <https://doi.org/10.1029/2012GL054031>
- 975
- 976 Attada, R., Kunchala, R. K., Dasari, H. P., Sivareddy, S., Yesubabu, V., Knio, O., Hoteit, I. (2021)
977 Representation of Arabian Peninsula summer climate in a regional atmospheric model using spectral
978 nudging. *Theoretical and Applied Climatology*, 145, 13-30. <https://doi.org/10.1007/s00704-021-03617-w>
- 979
- 980 AWI (2024). WRMC-BSRN: World Radiation Monitoring Center - Baseline Surface Radiation Network
981 [Dataset]. Accessed on 15 April 2024, available online at <https://bsrn.awi.de/>.
- 982
- 983 Barber, D. G., Massom, R. A. (2007) The Role of Sea Ice in Arctic and Antarctic Polynyas. In W. O. Smith
984 and D. G. Barber (Editors), *Polynyas: Windows to the World's Oceans*, pp. 1-54. Elsevier. Amsterdam.
- 985
- 986 Bowman, K. P. (2005) An Introduction to Programming with IDL: Interactive Data Language [Software].
987 Academic Press, 304 pp.. ISBN-10: 012088559X, ISBN-13: 978-0120885596.
- 988
- 989 Box, J. E., Nielsen, K. P., Yang, X., Niwano, M., Wehrle, A., van As, D., Fettweis, X., Koltzow, M. A. O.,
990 Palmason, B., Fausto, R. S., van den Broeke, M. R., Huai, B., Ahlstrom, A. P., Langley, K., Dachauer, A.,
991 Noel, B. (2023) Greenland ice sheet rainfall climatology, extremes and atmospheric river rapids.
992 *Meteorological Applications*, 30, e2134. <https://doi.org/10.1002/met.2134>
- 993
- 994 Bozkurt, D., Rondanelli, R., Marin, J. C., Garreaud, R. (2018) Foehn event triggered by an atmospheric
995 river underlies record-setting temperature along continental Antarctica. *Journal of Geophysical Research: Atmospheres*, 123, 3871-3892. <https://doi.org/10.1002/2017JD027796>
- 996
- 997
- 998 Bromwich, D. H., Otieno, F. O., Hines, K. M., Manning, K. W., Shilo, E. (2013) Comprehensive evaluation
999 of polar weather research and forecasting model performance in the Antarctic. *Journal of Geophysical
1000 Research: Atmospheres*, 118, 274-292. <https://doi.org/10.1029/2012JD018139>
- 1001
- 1002 Bromwich, D. H., Powers, J. G., Manning, K. W., Zou, X. (2022) Antarctic data impact experiments with
1003 Polar WRF during the YOPP-SH summer special observing period. *Quarterly Journal of the Royal
1004 Meteorological Society*, 148, 2194-2218. <https://doi.org/10.1002/qj.4298>
- 1005
- 1006 Chen, F., Dudhia, J. (2001) Coupling an Advanced Land Surface-Hydrology Model with the Penn State -
1007 NCAR MM5 Modeling System. Part I: Model Implementation and Sensitivity. *Monthly Weather Review*,
1008 129, 569-585. [https://doi.org/10.1175/1520-0493\(2001\)129<0569:CAALSH>2.0.CO;2](https://doi.org/10.1175/1520-0493(2001)129<0569:CAALSH>2.0.CO;2)
- 1009

- 1010 Chinta, S., Balaji, C. (2020) Calibration of WRF model parameters using multiobjective adaptive surrogate
1011 model-based optimization to improve the prediction of the Indian summer monsoon. *Climate Dynamics*,
1012 55, 631-650. <https://doi.org/10.1007/s00382-020-05288-1>
- 1013
- 1014 Dare, R. A., Budd, W. F. (2001) Analysis of Surface Winds at Mawson, Antarctica. *Weather and*
1015 *Forecasting*, 16, 416-431. [https://doi.org/10.1175/1520-0434\(2001\)016<0416:AOSWAM>2.0.CO;2](https://doi.org/10.1175/1520-0434(2001)016<0416:AOSWAM>2.0.CO;2)
- 1016
- 1017 Djoumna, G., Holland, D. M. (2021) Atmospheric rivers, warm air intrusions, and surface radiation balance
1018 in the Amundsen Sea Embayment. *Journal of Geophysical Research: Atmospheres*, 126, e2020JD034119.
1019 <https://doi.org/10.1029/2020JD034119>
- 1020
- 1021 Dery, S. J., Yau, M. K. (2002) Large-scale mass balance effects of blowing snow and surface sublimation.
1022 *Journal of Geophysical Research*, 107, 4679. <https://doi.org/10.1029/2001JD001251>
- 1023
- 1024 Dong, X., Wang, Y., Hou, S., Ding, M., Yin, B., Zhang, Y. (2020) Robustness of the Recent Global
1025 Atmospheric Reanalyses for Antarctic Near-Surface Wind Speed Climatology. *Journal of Climate*, 33,
1026 4027-4043. <https://doi.org/10.1175/JCLI-D-19-0648.1>
- 1027
- 1028 Eayrs, C., Holland, D. M., Francis, D., Wagner, T. J. W., Kumar, R., Li, X. (2019) Understanding the
1029 seasonal cycle of Antarctic sea ice extent in the context of long-term variability. *Reviews of Geophysics*,
1030 57, 1037-1064. <https://doi.org/10.1029/2018RG000631>
- 1031
- 1032 Eayrs, C., Li, X., Raphael, M. N., Holland, D. M. (2021) Rapid decline in Antarctic sea ice in recent years
1033 hints at future change. *Nature Geosciences*, 14, 460-464. <https://doi.org/10.1038/s41561-021-00768-3>
- 1034
- 1035 Elvidge, A. D., Munneke, K., King, P., Renfrew, I. A., Gilbert, E. (2020) Atmospheric drivers of melt on
1036 Larsen C Ice Shelf: Surface energy budget regimes and the impact of foehn. *Journal of Geophysical*
1037 *Research: Atmospheres*, 125, e2020JD032463. <https://doi.org/10.1029/2020JD032463>
- 1038
- 1039 England, M. R., Wagner, T. J. W., Eisenman, I. (2020) Modeling the breakup of tabular icebergs. *Science*
1040 *Advances*, 6, 51. <https://doi.org/10.1126/sciadv.abd1273>
- 1041
- 1042 EUMETSAT (2024) Ocean and Sea Ice Satellite Application Facility. Accessed on 12 August 2024,
1043 available online at <https://osi-saf.eumetsat.int/products/osi-405-c>
- 1044
- 1045 Feng, Z., Leung, L. R., Liu, N., Wang, J., Houze, R. A. Jr., Li, J., Hardin, J. C., Chen, D., Guo, J. (2021) A
1046 global high-resolution mesoscale convective system database using satellite-derived cloud tops, surface
1047 precipitation, and tracking. *Journal of Geophysical Research: Atmospheres*, 126, e2020JD034202.
1048 <https://doi.org/10.1029/2020JD034202>
- 1049
- 1050 Finlon, J. A., Rauber, R. M., Wu, W., Zaremba, T. J., McFarquhar, G. M., Nesbitt, S. W., Schnaiter, M.,
1051 Jarvinen, E., Waitz, F., Hill, T. C. J., DeMott, P. J. (2020) Structure of an atmospheric river over Australia
1052 and the Southern Ocean: II. Microphysical evolution. *Journal of Geophysical Research: Atmospheres*, 125,
1053 e2020JD032514. <https://doi.org/10.1029/2020JD032514>

- 1054
1055 Fogt, R. L., Bromwich, D. H., Hines, K. M. (2011) Understanding the SAM influence on the South Pacific
1056 ENSO teleconnection. *Climate Dynamics*, 36, 1555-1576. <https://doi.org/10.1007/s00382-010-0905-0>
1057
1058 Fons, S., Kurtz, N., Bagnardi, M. (2023) A decade-plus of Antarctic sea ice thickness and volume estimates
1059 from CryoSat-2 using a physical model and waveform fitting. *The Cryosphere*, 17, 2487-2508.
1060 <https://doi.org/10.5194/tc-17-2487-2023>
1061
1062 Fonseca, R., Francis, D., Aulicino, G., Mattingly, K., Fusco, G., Budillon, G. (2023) Atmospheric controls
1063 on the Terra Nova Bay polynya occurrence in Antarctica. *Climate Dynamics*, 61, 5147-5169.
1064 <https://doi.org/10.1007/s00382-023-06845-0>
1065
1066 Francis, D., Eayrs, C., Cuesta, J., Holland, D. (2019) Polar cyclones at the origin of the reoccurrence of the
1067 Maud Rise Polynya in austral winter 2017. *Journal of Geophysical Research: Atmospheres*, 124, 5251-
1068 5267. <https://doi.org/10.1029/2019JD030618>
1069
1070 Francis, D., Fonseca, R., Bozkurt, D., Nelli, N., Guan, B. (2024) Atmospheric River Rapids and Their Role
1071 in the Extreme Rainfall Event of April 2023 in the Middle East. *Geophysical Research Letters*, 51,
1072 e2024GL109446. <https://doi.org/10.1029/2024GL109446>
1073
1074 Francis, F., Fonseca, R., Mattingly, K. S., Lhermitte, S., Walker, C. (2023) Foehn winds at Pine Island
1075 Glacier and their role in ice changes. *The Cryosphere*, 17, 3041-3062. <https://doi.org/10.5194/tc-17-3041-2023>
1077
1078 Francis, D., Fonseca, R., Nelli, N., Bozkurt, D., Picard, G., Guan, B. (2022a) Atmospheric rivers drive
1079 exceptional Saharan dust transport towards Europe. *Atmospheric Research*, 266, 105959.
1080 <https://doi.org/10.1016/j.atmosres.2021.105959>
1081
1082 Francis, D., Mattingly, K. S., Lhermitte, S., Temimi, M., Heil, P. (2021) Atmospheric extremes caused high
1083 oceanward sea surface slope triggering the biggest calving event in more than 50 years at the Amery Ice
1084 Shelf. *The Cryosphere*, 15, 2147-2165. <https://doi.org/10.5194/tc-15-2147-2021>
1085
1086 Francis, D., Fonseca, R., Mattingly, K. S., Marsh, O. J., Lhermitte, S., Cherif, C. (2022b) Atmospheric
1087 triggers of the Brunt Ice Shelf calving in February 2021. *Journal of Geophysical Research: Atmospheres*,
1088 127, e2021JD036424. <https://doi.org/10.1029/2021JD036424>
1089
1090 Francis, D., Mattingly, K. S., Temimi, M., Massom, R., Heil, P. (2020) On the crucial role of atmospheric
1091 rivers in the two major Weddell Polynya events in 1973 and 2017 in Antarctica. *Science Advances*, 6.
1092 <https://doi.org/10.1126/sciadv.abc2695>
1093
1094 Fraser, A. D., Wongpan, P., Langhorne, P. J., Klekociuk, A. R., Kusahara, K., Lannuzel, D., Massom, R.
1095 A., Meiners, K. M., Swadling, K. M., Atwater, D. P., Brett, G. M., Corkill, M., Dalman, L. A., Fiddes, S.,
1096 Granata, A., Guglielmo, L., Heil, P., Leonard, G. H., Mahoney, A. R., McMinn, A., van der Merwe, P.,

- 1097 Weldrick, C. K., Wienecke, B. (2023) Antarctic landfast sea ice: A review of its physics, biogeochemistry
1098 and ecology. *Reviews of Geophysics*, 61, e2022RG000770. <https://doi.org/10.1029/2022RG000770>
- 1099
- 1100 Gehring, J., Vignon, E., Billault-Roux, A. C., Ferrone, A., Protat, A., Alexander, S. P., Berne, A. (2022)
1101 Orographic flow influence on precipitation during an atmospheric river event at Davis, Antarctica. *Journal*
1102 *of Geophysical Research: Atmospheres*, 127, e2021JD035210. <https://doi.org/10.1029/2021JD035210>.
- 1103
- 1104 Ghiz, M.L., Scott, R. C., Vogelmann, A. M., Lenaerts, J. T. M., Lazzara, M., Lubin, D. (2021) Energetics
1105 of surface melt in West Antarctica. *The Cryosphere*, 15, 3459-3494. <https://doi.org/10.5194/tc-15-3459-2021>
- 1106
- 1107
- 1108 Gilbert, E., Pishniak, D., Torres, J. A., Orr, A., Maclennan, M., Wever, N., Verro, K. (2025) Extreme
1109 precipitation associated with atmospheric rivers over West Antarctic ice shelves: insights from the
1110 kilometre-scale regional climate modeling. *The Cryosphere*, 19, 597-618. <https://doi.org/10.5194/tc-19-597-2025>
- 1111
- 1112
- 1113 Goosse, H., Contador, A., Bitz, C., Blanchard-Wrigglesworth, C. M., Eayrs, E., Fichefet, C., Himmich, T.,
1114 Huot, K., Klein, P.-V., Marchi, F., Massonnet, S., Mezzina, F., Pelletier, B., Roach, C., Vancoppenolle, L.,
1115 van Lipzig, N. P. M. (2023) Modulation of the seasonal cycle of the Antarctic sea ice extent by sea ice
1116 processes and feedbacks with the ocean and the atmosphere. *The Cryosphere*, 17, 407-425.
<https://doi.org/10.5194/tc-17-407-2023>
- 1117
- 1118
- 1119 Gorodetskaya, I. V., Duran-Alarcon, C., Gonzalez-Herrero, S., Clem, K. R., Zou, X., Rowe, P., Imazio, P.
1120 R., Campos, D., Leroy-Dos Santos, C., Dutrievoz, N., Wille, J. D., Chyhareva, A., Favier, V., Blanchet, J.,
1121 Pohl, B., Cordero, R. R., Prak, S.-J., Colwell, S., Lazzara, M. A., Carrasco, J., Gulisano, A. M., Krakovska,
1122 S., Ralph, F. M., Dethinne, T., Picard, G. (2023) Record-high Antarctic Peninsula temperatures and surface
1123 melt in February 2022: a compound event with an intense atmospheric river. *Npj Climate and Atmospheric*
1124 *Science*, 6, 202. <https://doi.org/10.1038/s41612-023-00529-6>
- 1125
- 1126 Gorodetskaya, I. V., Silva, T., Schmithusen, H., Hirasawa, N. (2020) Atmospheric river signatures in
1127 radiosonde profiles and reanalyses at the Dronning Maud Land Coast, East Antarctica. *Advances in*
1128 *Atmospheric Sciences*, 37, 455-476. <https://doi.org/10.1007/s00376-020-9221-8>
- 1129
- 1130 Gorodetskaya, I. V., Van Lipzig, N. P. M., Van den Broeke, M. R., Mangold, A., Boot, W., Reijmer, C. H.
1131 (2013) Meteorological regimes and accumulation patterns at Utsteinen, Dronning Maud Land, East
1132 Antarctica: Analysis of two contrasting years. *Journal of Geophysical Research: Atmospheres*, 118, 1700-
1133 1715. <https://doi.org/10.1002/jgrd.50177>
- 1134
- 1135 Gossart, A., Helsen, S., Lenaerts, J. T. M., Vanden Broucke, S., van Lipzig, N. P. M., Souverijns, N. (2019)
1136 An Evaluation of Surface Climatology in State-of-the-Art Reanalyses over the Antarctic Ice Sheet. *Journal*
1137 *of Climate*, 32, 6899-6915. <https://doi.org/10.1175/JCLI-D-19-0030.1>
- 1138

- 1139 Guest, P. S. (2021) Inside katabatic winds over the Terra Nova Bay polynya: 2. Dynamic and
1140 thermodynamic analyses. *Journal of Geophysical Research: Atmospheres*, 126, e2021JD034904.
1141 <https://doi.org/10.1029/2021JD034904>
- 1142
- 1143 Haas, C. (2017) Sea ice thickness distribution. In: *Sea Ice*, D. N. Thomas (Ed.). Blackwell Science.
1144 <https://doi.org/10.1002/9781118778371.ch2>
- 1145
- 1146 Haumann, F. A., Gruber, N., Munnich, M., Frenger, I., Kern, S. (2016) Sea-ice transport driving Southern
1147 Ocean salinity and its recent trends. *Nature*, 537, 89-92. <https://doi.org/10.1038/nature19101>
- 1148
- 1149 Heil, P. (2006) Atmospheric conditions and fast ice at Davis, East Antarctica: A case study. *Journal of*
1150 *Geophysical Research*, 111, C05009. <https://doi.org/10.1029/2005JC002904>
- 1151
- 1152 Heil, P., Allison, I., Lytle, V. I. (1996) Seasonal and interannual variations of the oceanic heat flux under a
1153 landfast Antarctic sea ice cover. *Journal of Geophysical Research*, 101(C11), 25741-25752.
1154 <https://doi.org/10.1029/96JC01921>
- 1155
- 1156 Hersbach, H., Bell, B., Berrisford, P., Biavati, G., Horanyi, A., Munoz Sabater, J., Nicolas, J., Peavey, C.,
1157 Radu, R., Rozum, I., Schepers, D., Simmons, A., Soci, C., Dee, D., Thepaut, J.-N. (2023a) ERA5 hourly
1158 data on single levels from 1940 to present [Dataset]. Copernicus Climate Change Service (C3S) Climate
1159 Data Store (CDS). Accessed on 22 April 2024, available online at <https://doi.org/10.24381/cds.adbb2d47>
- 1160
- 1161 Hersbach, H., Bell, B., Berrisford, P., Biavati, G., Horanyi, A., Munoz Sabater, J., Nicolas, J., Peavey, C.,
1162 Radu, R., Rozum, I., Schepers, D., Simmons, A., Soci, C., Dee, D., Thepaut, J.-N. (2023b) ERA5 hourly
1163 data on pressure levels from 1940 to present [Dataset]. Copernicus Climate Change Service (C3S) Climate
1164 Data Store (CDS). Accessed on 22 April 2024, available online at <https://doi.org/10.24381/cds.bd0915c6>
- 1165
- 1166 Hersbach, H., Bell, B., Berrisford, P., Hirahara, S., Horanyi, A., Munoz-Sabater, J., Nicolas, J., Peavey, C.,
1167 Radu, R., Schepers, D., Simmons, A., Soci, C., Abdalla, S., Abellana, X., Balsamo, G., Bechtold, P., Biavati,
1168 G., Bidiot, J., Bonavita, M., De Chiara, G., Dahlgren, P., Dee, D., Diamantakis, M., Dragani, R., Fleming,
1169 J., Forbes, R., Fuentes, M., Geer, A., Haimberger, L., Healy, S., Hogan, R. J., Holm, E., Janiskova, M.,
1170 Keeley, S., Laloyaux, P., Lopez, P., Lulu, C., Radnoti, G., de Rosnay, P., Rozum, I., Vamborg, F., Villaume,
1171 S., Thepaut, J.-N. (2020) The ERA5 global reanalysis. *Quarterly Journal of the Royal Meteorological*
1172 *Society*, 146, 1999-2049. <https://doi.org/10.1002/qj.3803>
- 1173
- 1174 Hines, K. M., Bromwich, D. H., Silber, I., Russell, L. M., Bai, L. (2021) Predicting frigid mixed-phase
1175 clouds for pristine coastal Antarctica. *Journal of Geophysical Research: Atmospheres*, 126,
1176 e2021JD035112. <https://doi.org/10.1029/2021JD035112>
- 1177
- 1178 Hines, K. M., Bromwich, D. H., Wang, S.-H., Silber, I., Verlinde, J., Lubin, D. (2019) Microphysics of
1179 summer clouds in central West Antarctica simulated by the Polar Weather Research and Forecasting Model
1180 (WRF) an the Antarctic Mesoscale Prediction System (AMPS). *Atmospheric Chemistry and Physics*, 19,
1181 12431-12454. <https://doi.org/10.5194/acp-19-12431-2019>
- 1182

- 1183 Hobbs, W., Spence, P., Meyer, A., Schroeter, S., Fraser, A. D., Reid, P., Tian, R. T., Wang, Z., Liniger, G.,
1184 Doddridge, E. W., Boyd, P. W. (2024) Observational Evidence for a Regime Shift in Summer Antarctic
1185 Sea Ice. *Journal of Climate*, 37, 2263-2275. <https://doi.org/10.1175/JCLI-D-23-0479.1>
- 1186
- 1187 Hoppmann, M., M. Nicolaus, P. A. Hunkeler, P. Heil, L.-K. Behrens, G. König-Langlo, R. Gerdes (2015)
1188 Seasonal evolution of an ice-shelf influenced fast-ice regime, derived from an autonomous thermistor chain.
1189 *Journal of Geophysical Research: Oceans*, 120, 1703–1724, <https://doi.org/10.1002/2014JC010327>.
- 1190
- 1191 Hoskins, B., Fonseca, R., Blackburn, M., Jung, T. (2012) Relaxing the Tropics to an ‘observed’ state:
1192 analysis using a simple baroclinic model. *Quarterly Journal of the Royal Meteorological Society*, 138, 1618–
1193 1626. <https://doi.org/10.1002/qj.1881>
- 1194
- 1195 Hoskins, B. J., Karoly, D. J. (1981) The Steady Linear Response of a Spherical Atmosphere to Thermal
1196 and Orographic Forcing. *Journal of Atmospheric Sciences*, 38, 1179-1196. [https://doi.org/10.1175/1520-0469\(1981\)038<1179:TSLROA>2.0.CO;2](https://doi.org/10.1175/1520-0469(1981)038<1179:TSLROA>2.0.CO;2)
- 1196
- 1197
- 1198 Hoskins, B. J., Valdes, P. J. (1990) On the Existence of Storm-Tracks. *Journal of Atmospheric Sciences*,
1199 47, 1854-1864. [https://doi.org/10.1175/1520-0469\(1990\)047<1854:OTEOST>2.0.CO;2](https://doi.org/10.1175/1520-0469(1990)047<1854:OTEOST>2.0.CO;2)
- 1200
- 1201
- 1202 Houze, R. A. Jr. (2004) Mesoscale convective systems. *Reviews of Geophysics*, 42, RG4003.
1203 <https://doi.org/10.1029/2004RG000150>
- 1204
- 1205 Hu, H., Zhao, J., Heil, P., Qin, Z., Ma, J., Hui, F., Cheng, X. (2023) Annual evolution of the ice-ocean
1206 interaction beneath landfast ice in Prydz Bay, East Antarctica. *The Cryosphere*, 17, 2231-2244.
1207 <https://doi.org/10.5194/tc-17-2231-2023>
- 1208
- 1209 Iacono, M. J., Delamere, J. S., Mlawer, E. J., Shephard, M. W., Clough, S. A., & Collins, W. D. (2008)
1210 Radiative forcing by long-lived greenhouse gasses: Calculations with the AER radiative transfer models.
1211 *Journal of Geophysical Research*, 113, D13103. <https://doi.org/10.1029/2008JD009944>
- 1212
- 1213 Jackson, K., J. Wilkinson, T. Maksym, D. Meldrum, J. Beckers, C. Haas, and D. Mackenzie (2013) A Novel
1214 and Low Cost Sea Ice Mass Balance Buoy. *Journal of Atmospheric and Oceanic Technology*, 30, 2676–
1215 2688. <https://doi.org/10.1175/JTECH-D-13-00058.1>
- 1216
- 1217 Kacimi, S., Kwok, R. (2020) The Antarctic sea ice cover from ICESat-2 and CryoSat-2: freeboard, snow
1218 depth, and ice thickness. *The Cryosphere*, 14, 4453-4474. <https://doi.org/10.5194/tc-14-4453-2020>
- 1219
- 1220 Kain, J. S. (2004) The Kain-Fritsch convective parameterization: An update. *Journal of Applied
1221 Meteorology*, 43, 170-181. [https://doi.org/10.1175/1520-0430\(2004\)043<0170:tkcpau>2.0.co;2](https://doi.org/10.1175/1520-0430(2004)043<0170:tkcpau>2.0.co;2)
- 1221
- 1222
- 1223 Kawamura, T., Takizawa, T., Ohshima, K. I., Ushio, S. (1995) Data of sea-ice cores obtained in Lutzow-
1224 Holm Bay from 1990 to 1992 (JARE-31, -32) in the period of Japanese Antarctic climate research. *JARE
1225 Data Rep.* 204 (Glaciol. 24), 42 pp., National Institute of Polar Research, Tokyo.
- 1226

- 1227 Koh, T.-Y., Wang, S., Bhatt, B. C. (2012) A diagnostic suite to assess NWP performance. *Journal of*
1228 *Geophysical Research*, 117, D13109. <https://doi.org/10.1029/2011JD017103>
- 1229
- 1230 Kuipers Munneke, P., McGrath, D., Medley, B., Luckman, A., Bevan, S., Kulessa, B., Jansen, D., Booth,
1231 A., Smeets, P., Hubbard, B., Ashmore, D., Van den Broeke, M., Sevestre, H., Steffen, K., Shepherd, A.,
1232 Gourmelen, N. (2017) Observationally constrained surface mass balance of Larsen C ice shelf, Antarctica.
1233 The Cryosphere, 11, 2411-2426. <https://doi.org/10.5194/tc-11-2411-2017>
- 1234
- 1235 Kurtz, N. T., Markus, T. (2012) Satellite observations of Antarctic sea ice thickness and volume. *Journal*
1236 *of Geophysical Research*, 117, C08025. <https://doi.org/10.1029/2012JC008141>
- 1237
- 1238 Lavergne, T., Eastwood, S., Teffah, Z., Schuberg, H., Breivik, L.-A. (2010) Sea ice motion from low-
1239 resolution satellite sensors: an alternative method and its validation in the Arctic. *Journal of Geophysical*
1240 *Research: Oceans*, 115, C10032. <https://doi.org/10.1029/2009JC005958>
- 1241
- 1242 Laffin, M. K., Zender, C. S., Singh, S., Van Wessem, J. M., Smeets, C. J. P. P., Reijmer, C. H. (2021)
1243 Climatology and evolution of the Antarctic Peninsula fohn wind-induced melt regime from 1979-2018.
1244 *Journal of Geophysical Research: Atmospheres*, 126, e2020JD033682.
1245 <https://doi.org/10.1029/2020JD033682>
- 1246
- 1247 Lazzara, M. (2024) Antarctic Meteorological Research Center & Automatic Weather Stations Project
1248 [Dataset]. Accessed on 12 May 2024, available online at <https://amrc.ssec.wisc.edu/>.
- 1249
- 1250 Lea, E. J., Jamieson, S. S. R., Bentley, M. J. (2024) Alpine topography of the Gamburtsev Subglacial
1251 Mountains, Antarctica, mapped from ice sheet surface morphology. *The Cryosphere*, 18, 1733-1751.
1252 <https://doi.org/10.5194/tc-18-1733-2024>
- 1253
- 1254 Li, H., Fedorov, A. V. (2021) Persistent freshening of the Arctic Ocean and changes in the North Atlantic
1255 salinity caused by Arctic sea ice decline. *Climate Dynamics*, 57, 2995-3013.
1256 <https://doi.org/10.1007/s00382-021-05850-5>
- 1257
- 1258 Li, X.-Q., Hui, F.-M., Zhao, J.-C., Zhai, M.-X., Cheng, X. (2022) Thickness simulation of landfast ice
1259 along Mawson Coast, East Antarctica based on a snow/ice high-resolution thermodynamic model.
1260 *Advances in Climate Change Research*, 13, 375-384. <https://doi.org/10.1016/j.accre.2022.05.005>
- 1261
- 1262 Liang, K., Wang, J., Luo, H., Yang, Q. (2023) The role of atmospheric rivers in Antarctic sea ice variations.
1263 *Geophysical Research Letters*, 50, e2022GL102588. <https://doi.org/10.1029/2022GL102588>
- 1264
- 1265 Liao, Z., Cheng, B., Zhao, J., Vihma, T., Jackson, K., Yang, Q., Yang, Y., Zhang, L., Li, Z., Qiu, Y., Cheng,
1266 X. (2018). Snow depth and ice thickness derived from SIMBA ice mass balance buoy data using an
1267 automated algorithm. *International Journal of Digital Earth*, 12(8), 962-979.
1268 <https://doi.org/10.1080/17538947.2018.1545877>
- 1269

- 1270 Liao, S., Luo, H., Wang, J., Shi, Q., Zhang, J., Yang, Q. (2022) An evaluation of Antarctic sea-ice thickness
1271 from the Global Ice-Ocean Modeling and Assimilation System based on it situ and satellite observations.
1272 The Cryosphere, 16, 1807-1819. <https://doi.org/10.5194/tc-16-1807-2022>
1273
- 1274 [Lim, S., Gim, H.-J., Lee, E., Lee, S., Lee, W. Y., Lee, Y. H., Cassardo, C., Park, S. K. \(2022\) Optimization](#)
1275 [of snow-related parameters in the Noah land surface model \(v3.4.1\) using a micro-genetic algorithm](#)
1276 [\(v1.7a\). Geoscientific Model Development, 15, 8541-8559. https://doi.org/10.5194/gmd-15-8541-2022](#)
1277
- 1278 [Liu, Y., Key, J. R., Wang, X., Tschudi, M. \(2020\) Multidecadal Arctic sea ice thickness and volume derived](#)
1279 [from ice age. The Cryosphere, 14, 1325-1345. https://doi.org/10.5194/tc-14-1325-2020](#)
1280
- 1281 Maksym, T., Markus, T. (2008) Antarctic sea ice thickness and snow-to-ice conversion from atmospheric
1282 reanalysis and passive microwave snow depth. Journal of Geophysical Research, 113, C02S12.
1283 <https://doi.org/10.1029/2006JC004085>
1284
- 1285 Maksym, T., Stammerjohn, S., Ackley, S., Massom, R. (2012) Antarctic sea ice – A polar opposite?
1286 Oceanography 25, 140-151. <https://doi.org/10.5670/oceanog.2012.88>
1287
- 1288 Marengo, J. A., Soares, W. R., Saulo, C., Nicolini, M. (2004) Climatology of the Low-Level Jet East of the
1289 Andes as Derived from the NCEP-NCAR Reanalyses: Characteristics and Temporal Variability. Journal of
1290 Climate, 17, 2261-2280. [https://doi.org/10.1175/1520-0442\(2004\)017<2261:COTLJE>2.0.CO;2](https://doi.org/10.1175/1520-0442(2004)017<2261:COTLJE>2.0.CO;2)
1291
- 1292 Marshall, G. J. (2003) Trends in the Southern Annular Mode from Observations and Reanalyses. Journal
1293 of Climate, 16, 4134-4143. [https://doi.org/10.1175/1520-0442\(2003\)016<4134:TSAM>2.0.CO;2](https://doi.org/10.1175/1520-0442(2003)016<4134:TSAM>2.0.CO;2)
1294
- 1295 Massom, R.A., H. Eicken, C. Haas, M.O. Jeffries, M.R. Drinkwater, M. Sturm, A.P. Worby, X. Wu, V.I.
1296 Lytle, S. Ushio, K. Morris, P.A. Reid, S. Warren, and I. Allison. (2001) Snow on Antarctic sea ice. Reviews
1297 of Geophysics, 39(3), 413-445. <https://doi.org/10.1029/2000RG000085>
1298
- 1299 Massom, R. A., Pook, M. J., Comiso, J. C., Adams, N., Turner, J., Lachlan-Cope, T., Gibson, T. T. (2004)
1300 Precipitation over the interior East Antarctic Ice Sheet related to mid-latitude blocking-high activity.
1301 Journal of Climate, 17, 1914-1928. [https://doi.org/10.1175/1520-0442\(2004\)017%3C1914:POTIEA%3E2.0.CO;2](https://doi.org/10.1175/1520-0442(2004)017%3C1914:POTIEA%3E2.0.CO;2)
1302
- 1303
- 1304 Massonnet, F., Mathiot, P., Fichefet, T., Goosse, H., Beatty, C. K., Vancopenolle, M., Lavergne, T. (2013)
1305 A model reconstruction of the Antarctic sea ice thickness and volume changes over 1980-2008 using data
1306 assimilation. Ocean Modeling, 64, 67-75. <https://doi.org/10.1016/j.ocemod.2013.01.003>
1307
- 1308 Matejka, M., Laska, K., Jeklova, K., Hosek, J. (2021) High-Resolution Numerical Modeling of Near-
1309 Surface Atmospheric Fields in the Complex Terrain of James Ross Island, Antarctic Peninsula.
1310 Atmosphere, 12, 360. <https://doi.org/10.3390/atmos12030360>
1311
- 1312 Mathworks (2024) Math. Graphics. Programming [Software]. Accessed on 18 March 2024, available online
1313 at <https://uk.mathworks.com/products/matlab.html>

- 1314
1315 McLennan, M. L., Lenaerts, J. T. M., Shields, C. A., Hoffman, A. O., Wever, N., Thompson-Munson, M.,
1316 Winters, A. C., Pettit, E. C., Scambos, T. A., Wille, J. D. (2023) Climatology and surface impacts of
1317 atmospheric rivers on West Antarctica. *The Cryosphere*, 17, 865-881. <https://doi.org/10.5194/tc-17-865-2023>
1318
1319
1320 McLennan, M. L., Lenaerts, J. T. M., Shields, C., Wille, J. D. (2022) Contribution of atmospheric rivers to
1321 Antarctic precipitation. *Geophysical Research Letters*, 49, e2022GL100585.
1322 <https://doi.org/10.1029/2022GL100585>
1323
1324 Meredith, M. P., Stammerjohn, S. E., Ducklow, H. W., Leng, M. J., Arrowsmith, C., Brearley, J. A.,
1325 Venables, H. J., Barham, M., van Wessem, J. M., Schofield, O., Waite, N. (2021) Local- and large-scale
1326 drivers of variability in the coastal freshwater budget of the Western Antarctic Peninsula. *Journal of*
1327 *Geophysical Research: Oceans*, 126, e2021JC017172. <https://doi.org/10.1029/2021JC017172>
1328
1329 Miles, B. W. J., Stokes, C. R., Jamieson, S. S. R. (2017) Simultaneous disintegration of outlet glaciers in
1330 Porpoise Bay (Wilkes Land), East Antarctica, driven by sea ice break-up. *The Cryosphere*, 11, 427-442.
1331 <https://doi.org/10.5194/tc-11-427-2017>
1332
1333 Mills, C. M. (2011) Modification of the Weather Research and Forecasting Model's treatment of sea ice
1334 albedo over the Arctic Ocean. WRF3.3.1 Code Submission Doc., 2 pp. Accessed on 19 August 2024,
1335 available online at
1336 http://publish.illinois.edu/catrinmills/files/2012/10/Mills_WRFIceAlbedoProj_Summary.pdf
1337
1338 Montini, T. L., Jones, C., Carvalho, L. M. V. (2019) The South American low-level jet: A new climatology,
1339 variability, and changes. *Journal of Geophysical Research: Atmospheres*, 124, 1200-1218.
1340 <https://doi.org/10.1029/2018JD029634>
1341
1342 Morrison, H., Milbrandt, J. A. (2015) Parameterization of Cloud Microphysics Based on the Prediction of
1343 Bulk Ice Particle Properties. Part I: Scheme Description and Idealized Tests. *Journal of the Atmospheric*
1344 *Sciences*, 72, 287-311. <https://doi.org/10.1175/JAS-D-14-0065.1>
1345
1346 Nakanishi, M., Niino, H. (2006) An improved Mellor-Yamada level-3 model: Its numerical stability and
1347 application to a regional prediction of advection fog. *Boundary-Layer Meteorology*, 119, 397-407.
1348 <https://doi.org/10.1007/s10546-005-9030-8>
1349
1350 Nelli, N. R., Francis, D., Fonseca, R., Abida, R., Weston, M., Wehbe, Y., Al Hosary, T. (2021) The
1351 atmospheric controls of extreme convective events over the southern Arabian Peninsula during the spring
1352 season. *Atmospheric Research*, 262, 105788. <https://doi.org/10.1016/j.atmosres.2021.105788>
1353
1354 [Niu, G.-Y., Yang, Z.-L., Mitchell, K. E., Chen, F., Ek, M. B., Barlage, M., Kumar, A., Manning, K., Niyogi, D., Rosero, E., Tewari, M., Xia, Y. \(2011\) The community Noah land surface model with multiparameterization options \(Noah-MP\): 1. Model description and evaluation with local-scale measurements. Journal of Geophysical Research, 116, D12109. https://doi.org/10.1029/2010JD015139](https://doi.org/10.1029/2010JD015139)
1355
1356
1357

- 1358
1359 NOAA ARL (2024) HYSPLIT for Linux - Public (unregistered) version download [Software]. National
1360 Oceanic and Atmospheric Administration Air Resources Laboratory. Accessed on 04 July, available online
1361 at https://www.ready.noaa.gov/HYSPLIT_linuxtri
1362
1363 NOAA/NWS (2024) Cold & Warm Episodes by Season [Dataset]. National Oceanic and Atmospheric
1364 Administration / National Weather Service Climate Prediction Center. Accessed on 24 July, available
1365 online at https://origin.cpc.ncep.noaa.gov/products/analysis_monitoring/ensostuff/ONI_v5.php
1366
1367 Oliveira, F. N. M., Carvalho, L. M. V., Ambrizzi, T. (2013) A new climatology for Southern Hemisphere
1368 blockings in the winter and the combine defect of ENSO and SAM phases. International Journal of
1369 Climatology, 34, 676-1692. <https://doi.org/10.1002/joc.3795>
1370
1371 Oolman, L. (2025) University of Wyoming - atmospheric soundings [Dataset]. Accessed on 04 July 2024,
1372 data available online at <https://weather.uwyo.edu/upperair/sounding.html>
1373
1374 Parkinson, C. L. (2019) A 40-y record reveals gradual Antarctic sea ice increases followed by decreases at
1375 rates far exceeding the rates seen in the Arctic. Environmental Sciences, 116, 14414-14423.
1376 <https://doi.org/10.1073/pnas.1906556116>
1377
1378 Parkinson, C. L., Cavalieri, D. J. (2012) Antarctic sea ice variability and trends, 1979-2010. The
1379 Cryosphere, 6, 871-880. <https://doi.org/10.5194/tc-6-871-2012>
1380
1381 Plante, M., Lemieux, J.-F., Tremblay, L. B., Tivy, A., Angnatok, J., Roy, F., Smith, G., Dupont, F., Turner,
1382 A. K. (2024) Using Icepak to reproduce ice mass balance buoy observations in landfast ice: improvements
1383 from the mushy-layer thermodynamics. The Cryosphere, 18, 1685-1708. <https://doi.org/10.5194/tc-18-1685-2024>
1385
1386 Pook, M. J., Risbey, J. S., McIntosh, P. C., Ummenhofer, C. C., Marshall, A. G., Meyers, G. A. (2013) The
1387 seasonal cycle of blocking and associated physical mechanisms in the Australian region and relationship
1388 with rainfall. Monthly Weather Review, 141, 4534-4553. <https://doi.org/10.1175/MWR-D-13-00040.1>
1389
1390 Purich, A., Doddridge, E. W. (2023) Record low Antarctic sea ice coverage indicates a new sea ice state.
1391 Communications Earth & Environment, 4, 314. <https://doi.org/10.1038/s43247-023-00961-9>
1392
1393 PWRF (2024) The Polar WRF. Byrd Polar and Climate Research Center. The Ohio State University
1394 [Model]. Accessed on 08 April 2024, available online at <https://polarmet.osu.edu/PWRF/>.
1395
1396 Quan, J., Di, Z., Duan, Q., Gong, W., Wang, C., Gan, Y., Ye, A., Miao, C. (2016) An evaluation of
1397 parametric sensitivities of different meteorological variables simulated by the WRF model. Quarterly
1398 Journal of the Royal Meteorological Society, 142, 2925-2934. <https://doi.org/10.1002/qj.2885>
1399

- 1400 Raphael, M. N., Hobbs, W., Wainer, I. (2011) The effect of Antarctic sea ice on the Southern Hemisphere
1401 atmosphere during the southern summer. *Climate Dynamics*, 36, 1403-1417.
1402 <https://doi.org/10.1007/s00382-010-0892-1>
- 1403
- 1404 Rauber, R., M., Hu, H., Dominguez, F., Nesbitt, S. W., McFarquhar, G. M., Zaremba, T. J., Finlon, J. A.
1405 (2020) Structure of an atmospheric river over Australia and the Southern Ocean. Part I: Tropical and
1406 midlatitude water vapor fluxes. *Journal of Geophysical Research: Atmospheres*, 125, e2020JD032513.
1407 <https://doi.org/10.1029/2020JD032513>
- 1408
- 1409 Reid, P., Stammerjohn, S., Massom, R. A., Barreira, S., Scambos, T., Lieser, J. L. (2024) Sea-ice extent,
1410 concentration, and seasonality [in “State of the Climate in 2023”]. *Bulletin of the American Meteorological
1411 Society*, 105, 350-353. <https://doi.org/10.1175/BAMS-D-24-0099.1>
- 1412
- 1413 Riihelä, A., Bright, R. M., Anttila, K. (2021) Recent strengthening of snow and ice albedo feedback driven
1414 by Antarctic sea-ice loss. *Nature Geosciences*, 14, 832-836. <https://doi.org/10.1038/s41561-021-00841-x>
- 1415
- 1416 Roach, L. A., Dorr, J., Holmes, C. R., Massonnet, F., BLockley, E. W., Notz, D., Rackow, T., Raphael, M.
1417 N., O’Farrell, S. P., Bailey, D. A., Bitz, C. M. (2020) Antarctic Sea Ice Area in CMIP6. *Geophysical
1418 Research Letters*, 47, e2019GL086729. <https://doi.org/10.1029/2019GL086729>
- 1419
- 1420 Schroeter, S., Sandery, P. A. (2022) Large-ensemble analysis of Antarctic sea ice model sensitivity to
1421 parameter uncertainty. *Ocean Modeling*, 177, 102090. <https://doi.org/10.1016/j.ocemod.2022.102090>
- 1422
- 1423 Sledd, A., Shupe, M. D., Solomon, A., Cox, C. J., Perovich, D., Lei, R. (2024) Snow thermal conductivity
1424 and conductive flux in the Central Arctic: Estimates from observations and implications for models.
1425 *Elements: Science of the Anthropocene*, 12, 00086. <https://doi.org/10.1525/elementa.2023.00086>
- 1426
- 1427 Skamarock, W. C., Klemp, J. B., Dudhia, J., Gill, D. O., Liu, Z., Berner, J., Wang, W., Powers, J. G., Duda,
1428 M. G., Barker, D., Huang, X.-Y. (2019) Description of the Advanced Research WRF Model Version 4.3
1429 (No. NCAR/TN-556+STR). Accessed on 03 June 2024, available online at
1430 <https://opensky.ucar.edu/islandora/object/opensky:2898>
- 1431
- 1432 Spreen, G., Kaleschke, L., Heygster, G. (2008) Sea ice remote sensing using AMSR-E 89-GHz channels.
1433 *Journal of Geophysical Research*, 113, C02S03. <https://doi.org/10.1029/2005JC003384>
- 1434
- 1435 Stein, A. F., Draxler, R. R., Rolph, G. D., Stunder, B. J. B., Cohen, M. D., Ngan, F. (2015) NOAA’s
1436 HYSPLIT atmospheric transport and dispersion modeling system. *Bulletin of the American Meteorological
1437 Society*, 96, 2059-2077. <https://doi.org/10.1175/BAMS-D-14-00110.1>
- 1438 Szapiro, N., Cavallo, S. (2018) TPVTrack v1.0: A watershed segmentation and overlap correspondence
1439 method for tracking tropopause polar vortices. *Geoscientific Model Development*, 11, 5173-5187.
1440 <https://doi.org/10.5194/gmd-11-5173-2018>

- 1441 Takaya, K., Nakamura, H. (2001) A Formulation of a Phase-Independent Wave-Activity Flux for Stationary
1442 and Migratory Quasigeostrophic Eddies on a Zonally Varying Basic Flow. *Journal of the Atmospheric*
1443 *Sciences*, 58, 608-627. [https://doi.org/10.1175/1520-0469\(2001\)058<0608:AFOAPI>2.0.CO;2](https://doi.org/10.1175/1520-0469(2001)058<0608:AFOAPI>2.0.CO;2)
- 1444 Tewari, M., Chen, F., Wang, W., Dudhia, J., Lemone, M. A., Mitchell, K. E., et al. (2004) Implementation
1445 and verification of the unified NOAH land surface model in the WRF model. *20th Conference on Weather*
1446 *Analysis and Forecasting/16th Conference on Numerical Weather Prediction*, Seattle, W, American
1447 Meteorological Society, 14.2.a. Accessed on 25 January 2024, available online at
1448 <https://opensky.ucar.edu/islandora/object/conference:1576>
- 1449 Tewari, K., Mishra, S. K., Salunke, P., Ozawa, H., Dewan, A. (2023) Potential effects of the projected
1450 Antarctic sea-ice loss on the climate system. *Climate Dynamics*, 60, 589-601.
1451 <https://doi.org/10.1007/s00382-022-06320-2>
- 1452 Thomas, D (editor) (2017) Sea Ice. 3rd Edition. Wiley-Blackwell, New York (USA) and Oxford (UK), 664
1453 pp. ISBN: 978-1-118-77838-8.
- 1454 Terpstra, A., Gorodetskaya, I. V., Sodemann, H. (2021) Linking sub-tropical evaporation and extreme
1455 precipitation over East Antarctica: An atmospheric river case study. *Journal of Geophysical Research: Atmospheres*, 126, e2020JD033617. <https://doi.org/10.1029/2020JD033617>
- 1457 Trusel, L. D., Kromer, J. D., Datta, R. T. (2023) Atmospheric Response to Antarctic Sea-Ice Reductions
1458 Drives Ice Sheet Surface Mass Balance Increase. *Journal of Climate*, 19, 6879-6896.
1459 <https://doi.org/10.1175/JCLI-D-23-0056.1>
- 1460 University of Bremen (UoB) (2024) Sea Ice Remote Sensing, Data Archived. Accessed on 01 August 2024,
1461 available online at <https://data.seaice.uni-bremen.de/>.
- 1462 Vignon, E., Alexander, S. P., DeMott, P. J., Sotiropoulou, G., Gerber, F., Hill, T. C. J., Marchand, R.,
1463 Nenes, A., Berne, A. (2021) Challenging and improving the simulation of mid-level mixed-phase clouds
1464 over the high-latitude Southern Ocean. *Journal of Geophysical Research: Atmospheres*, 126,
1465 e2020JD033490. <https://doi.org/10.1029/2022JD033490>
- 1466 Vignon, E., Traulle, O., Berne, A. (2019) On the fine vertical structure of the low troposphere over coastal
1467 margins of East Antarctica. *Atmospheric Chemistry and Physics*, 19, 4659-4683.
1469 <https://doi.org/10.5194/acp-19-4659-2019>
- 1471 Wallace, J. M., Hobbs, P. V. (2006) Atmospheric science: An introductory survey. 504 pp. Academic Press
1472 Inc., second edition. ISBN-10: 012732951X, ISBN-13: 978-0127329512.
- 1473 Wang, Z., Li, Z., Zeng, J., Liang, S., Zhang, P., Tang, F., Chen, S., Ma, X. (2020) Spatial and temporal
1474 variations of Arctic sea ice from 2002 to 2017. *Earth and Space Science*, 7, e2020EA001278.
1476 <https://doi.org/10.1029/2020EA001278>
- 1477

- 1478 Wang, M., Linhardt, F., Lion, V., Oppelt, N. (2024) Melt Pond Evolution along the MOSAiC Drift:
1479 Insights from Remote Sensing and Modeling. *Remote Sensing*, 16, 3748.
1480 <https://doi.org/10.3390/rs16193748>
- 1481
- 1482 Wang, J., Massonnet, F., Goosse, H., Luo, H., Barthelemy, A., Wang, Q. (2024) Synergistic atmosphere-
1483 ocean-ice influences have driven the 2023 all-time Antarctic sea-ice record low. *Communications Earth &*
1484 *Environment*, 5, 415. <https://doi.org/10.1038/s43247-024-01523-3>
- 1485
- 1486 Webster, M., Gerland, S., Holland, M., Hunke, E., Kwok, R., Lecomte, O., Masson, R., Perovich, D., Sturm,
1487 M. (2018) Snow in the changing sea-ice system. *Nature Climate Change*, 8, 945-954.
1488 <https://doi.org/10.1038/s41558-018-0286-7>
- 1489
- 1490 Wille, J. D., Alexander, S. P., Amory, C., Baiman, R., Barthelemy, L., Bergstrom, D. M., Berne, A., Binder,
1491 H., Blanchet, J., Bozkurt, D., Bracegirdle, T. J., Casado, M., Choi, T., Clem, K. R., Cordron, F., Datta, R.,
1492 Di Battista, S., Favier, V., Francis, D., Fraser, A. D., Fourre, E., Garreaud, R. D., Genthon, C.,
1493 Goorodetskaya, I. V., Gonzalez-Herrero, S., Heinrich, V. J., Hubert, G., Joos, H., Kim, S.-J., King, J. C.,
1494 Kittel, C., Landais, A., Lazzara, M., Leonard, G. H., Lieser, J. L., Maclennan, M., Mikolajczyk, D., Neff,
1495 P., Ollivier, I., Picard, G., Pohl, B., Ralph, F. M., Rowe, P., Schlosser, E., Shields, C. A., Smith, I. J.,
1496 Sprenger, M., Trusel, L., Udy, D., Vance, T., Vignon, E., Walker, C., Wever, N., Zou, X. (2024a) The
1497 Extraordinary March 2022 East Antarctica “Heat” Wave. Part I: Observations and Meteorological Drivers.
1498 *Journal of Climate*, 37, 757-778. <https://doi.org/10.1175/JCLI-D-23-0175.1>
- 1499
- 1500 Wille, J. D., Alexander, S. P., Amory, C., Baiman, R., Barthelemy, L., Bergstrom, D. M., Berne, A., Binder,
1501 H., Blanchet, J., Bozkurt, D., Bracegirdle, T. J., Casado, M., Choi, T., Clem, K. R., Cordron, F., Datta, R.,
1502 Di Battista, S., Favier, V., Francis, D., Fraser, A. D., Fourre, E., Garreaud, R. D., Genthon, C.,
1503 Goorodetskaya, I. V., Gonzalez-Herrero, S., Heinrich, V. J., Hubert, G., Joos, H., Kim, S.-J., King, J. C.,
1504 Kittel, C., Landais, A., Lazzara, M., Leonard, G. H., Lieser, J. L., Maclennan, M., Mikolajczyk, D., Neff,
1505 P., Ollivier, I., Picard, G., Pohl, B., Ralph, F. M., Rowe, P., Schlosser, E., Shields, C. A., Smith, I. J.,
1506 Sprenger, M., Trusel, L., Udy, D., Vance, T., Vignon, E., Walker, C., Wever, N., Zou, X. (2024b) The
1507 Extraordinary March 2022 East Antarctica “Heat” Wave. Part II: Impacts on the Antarctic Ice Sheet. *Journal*
1508 *of Climate*, 37, 779-799. <https://doi.org/10.1175/JCLI-D-23-0176.1>
- 1509
- 1510 Wille, J. D., Bromwich, D. H., Cassano, J. J., Nigro, M. A., Mateling, M. E., Lazzara, M. A. (2017)
1511 Evaluation of the AMPS Boundary Layer Simulations on the Ross Ice Shelf, Antarctica, with Unmanned
1512 Aircraft Observations. *Journal of Applied Meteorology and Climatology*, 56, 2239-2258.
1513 <https://doi.org/10.1175/JAMC-D-16-0339.1>
- 1514
- 1515 Wille, J. D., Bromwich, D. H., Nigro, M. A., Cassano, J. J., Mateling, M., Lazzara, M. A., Wang, S.-H.
1516 (2016) Evaluation of the AMPS Boundary Layer Simulations on the Ross Ice Shelf with Tower
1517 Observations. *Journal of Applied Meteorology and Climatology*, 55, 2349-2367.
1518 <https://doi.org/10.1175/JAMC-D-16-0032.1>
- 1519

- 1520 Wille, J. D., Favier, V., Dufour, A., Gorodetskaya, I. V., Turner, J., Agosta, C., Codron, F. (2019) West
1521 Antarctic surface melt triggered by atmospheric rivers. *Nature Geoscience*, 12, 911-916.
1522 <https://doi.org/10.1038/s41561-019-0460-1>
- 1523
- 1524 Wille, J. D., Favier, V., Gorodetskaya, I. V., Agosta, C., Baiman, R., Barrett, J. E., Barthelemy, L., Boza,
1525 B., Bozkurt, D., Casado, M., Chyhareva, A., Clem, K. R., Codron, F., Datta, R. T., Duran-Alarcon, C.,
1526 Francis, D., Hoffman, A. O., Kolbe, M., Krakosvska, S., Linscott, G., Maclennan, M. L., Mattingly, K. S.,
1527 Mu, Y., Pohl, B., Santos, C. L.-D., Shields, C. A., Toker, E., Winters, A. C., Yin, Z., Zou, X., Zhang, C.,
1528 Zhang, Z. (2025) Atmospheric rivers in Antarctica. *Nature Reviews Earth & Environment*, 6, 178-192.
1529 <https://doi.org/10.1038/s43017-024-00638-7>
- 1530
- 1531 Wille, J. D., Favier, V., Gorodetskaya, I. V., Agosta, C., Kittel, C., Beeman, J. C., Jourdain, N. C., Lenaerts,
1532 J. T. M., Codron, F. (2021) Antarctic atmospheric river climatology and precipitation impacts. *Journal of*
1533 *Geophysical Research: Atmospheres*, 126, e2020JD033788. <https://doi.org/10.1029/2020JD033788>
- 1534
- 1535 Wille, J. D., Pohl, B., Favier, V., Winters, A. C., Baiman, R., Cavallo, S. M., Leroy-Dos Santos, C., Clem,
1536 K., Udy, D. G., Vance, T. R., Gorodetskaya, I., Codron, F., Berchet, A. (2024c) Examining atmospheric
1537 river life cycles in East Antarctica. *Journal of Geophysical Research: Atmospheres*, 129, e2023JD039970.
1538 <https://doi.org/10.1029/2023JD039970>
- 1539
- 1540 Williams, N., Byrne, N., Feltham, D., Van Leeuwen, P. J., Bannister, R., Schroeder, D., Ridout, A., Nerger,
1541 L. (2023) The effects of assimilating a sub-grid-scale sea ice thickness distribution in a new Arctic sea ice
1542 data assimilation system. *The Cryosphere*, 17, 2509-2532. <https://doi.org/10.5194/tc-17-2509-2023>
- 1543
- 1544 Worby, A. P., Steer, A., Lieser, J. L., Heil, P., Yi, D., Markus, T., Allison, I., Massom, R. A., Galin, N.,
1545 Zwally, J. (2011) Regional-scale sea-ice and snow thickness distribution from in situ and satellite
1546 measurements over East Antarctica during SIPEX 2007. *Deep Sea Research Part II: Topical Studies in*
1547 *Oceanography*, 58, 1125-1136. <https://doi.org/10.1016/j.dsr2.2010.12.001>
- 1548
- 1549 Xie, H., Ackley, S. F., Yi, D., Zwally, H. J., Wagner, P., Weissling, B., Lewis, M., Ye, K. (2011) Sea-ice
1550 thickness distribution of the Bellingshausen Sea from surface measurements and ICESat altimetry. *Deep*
1551 *Sea Research Part II: Topical Studies in Oceanography*, 58, 1039-1051.
1552 <https://doi.org/10.1016/j.dsr2.2010.10.038>
- 1553
- 1554 Xue, J., Xiao, Z., Bromwich, D. H., Bai, L. (2022) Polar WRF V4.1.1 simulation and evaluation for the
1555 Antarctic and Southern Ocean. *Frontiers of Earth Science*, 16, 1005-1024. <https://doi.org/10.1007/s11707-022-0971-8>
- 1556
- 1557
- 1558 Yang, J., Xiao, X., Liu, J., Li, Qin, D. (2021) Variability of Antarctic sea ice extent over the past 200 years.
1559 *Science Bulletin*, 66, 2394-2404. <https://doi.org/10.1016/j.scib.2021.07.028>
- 1560
- 1561 Zhang, J. (2014) Modeling the Impact of Wind Intensification on Antarctic Sea Ice Volume. *Journal of*
1562 *Climate*, 27, 202-214. <https://doi.org/10.1175/JCLI-D-12-00139.1>
- 1563

- 1564 Zhang, R., Screen, J. A. (2021) Diverse Eurasian winter temperature responses to Barents-Kara sea ice
1565 anomalies of different magnitudes and seasonality. *Geophysical Research Letters*, 48, e2021GL092726.
1566 <https://doi.org/10.1029/2021GL092726>
- 1567
- 1568 Zeng, X., Beljaars, A. (2005) A prognostic scheme of sea surface skin temperature for modeling and data
1569 assimilation. *Geophysical Research Letters*, 32, L14605. <https://doi.org/10.1029/2005GL023030>
- 1570
- 1571 Zou, X., Bromwich, D. H., Montenegro, A., Wang, S.-H., Bai, L. (2021a) Major surface melting over the
1572 Ross Ice Shelf part I: Foehn effect. *Quarterly Journal of the Royal Meteorological Society*, 147, 2874-2894.
1573 <https://doi.org/10.1002/qj.4104>
- 1574
- 1575 Zou, X., Bromwich, D. H., Montenegro, A., Wang, S.-H., Bai, L. (2021b) Major surface melting over the
1576 Ross Ice Shelf part II: Surface energy balance. *Quarterly Journal of the Royal Meteorological Society*, 147,
1577 2895-2916. <https://doi.org/10.1002/qj.4105>
- 1578
- 1579 Zou, X., Rowe, P. M., Gorodetskaya, I., Bromwich, D. H., Lazzara, M. A., Cordero, R. R., Zhang, Z.,
1580 Kawzenuk, B., Cordeira, J. M., Wille, J. D., Ralph, F. M., Bai, L.-S. (2023) Strong warming over the
1581 Antarctic Peninsula during combined atmospheric River and foehn events: Contribution of shortwave
1582 radiation and turbulence. *Journal of Geophysical Research: Atmospheres*, 128, e2022JD038138.
1583 <https://doi.org/10.1029/2022JD038138>